Monthly Notices
of the
ROYAL ASTRONOMICAL SOCIETY

MNRAS **505,** 5142–5163 (2021) https://doi.org/10.1093/mnras/stab1295
Advance Access publication 2021 May 7

The interplay between ambipolar diffusion and Hall effect on magnetic field decoupling and protostellar disc formation

Bo Zhao [1,2★†] Paola Caselli,[1] Zhi-Yun Li,[3] Ruben Krasnopolsky,[4] Hsien Shang[4] and Ka Ho Lam [3]
[1] *Max-Planck-Institut für extraterrestrische Physik (MPE), D-85748 Garching, Germany*
[2] *Department of Physics & Astronomy, McMaster University, Hamilton, ON L8S 4K1, Canada*
[3] *Astronomy Department, University of Virginia, Charlottesville, VA 22904, USA*
[4] *Academia Sinica Institute of Astronomy and Astrophysics, 10167 Taipei, Taiwan*

Accepted 2021 May 4. Received 2021 May 3; in original form 2020 September 17

ABSTRACT

Non-ideal magnetohydrodynamic (MHD) effects have been shown recently as a robust mechanism of averting the magnetic braking 'catastrophe' and promoting protostellar disc formation. However, the magnetic diffusivities that determine the efficiency of non-ideal MHD effects are highly sensitive to microphysics. We carry out non-ideal MHD simulations to explore the role of microphysics on disc formation and the interplay between ambipolar diffusion (AD) and Hall effect during the protostellar collapse. We find that removing the smallest grain population ($\lesssim$10 nm) from the standard MRN size distribution is sufficient for enabling disc formation. Further varying the grain sizes can result in either a Hall-dominated or an AD-dominated collapse; both form discs of tens of au in size regardless of the magnetic field polarity. The direction of disc rotation is bimodal in the Hall-dominated collapse but unimodal in the AD-dominated collapse. We also find that AD and Hall effect can operate either with or against each other in both radial and azimuthal directions, yet the combined effect of AD and Hall is to move the magnetic field radially outward relative to the infalling envelope matter. In addition, microphysics and magnetic field polarity can leave profound imprints both on observables (e.g. outflow morphology, disc to stellar mass ratio) and on the magnetic field characteristics of protoplanetary discs. Including Hall effect relaxes the requirements on microphysics for disc formation, so that prestellar cores with cosmic ray ionization rate of $\lesssim$2–3 $\times$ 10^{-16} s^{-1} can still form small discs of $\lesssim$10 au radius. We conclude that disc formation should be relatively common for typical prestellar core conditions, and that microphysics in the protostellar envelope is essential to not only disc formation, but also protoplanetary disc evolution.

Key words: magnetic fields – MHD – circumstellar matter – stars: formation.

1 INTRODUCTION

Protostellar disc formation is a critical step between the collapse of dense molecular cores and the formation of stars and planets. How rotationally supported discs (RSDs hereafter) are formed from magnetized dense cores remains an unsettled question in existing literature. The main debate is on how to avert the 'catastrophic' magnetic braking that transports away angular momentum from the circumstellar region and hence suppresses disc formation (Allen, Li & Shu 2003; Hennebelle & Fromang 2008; Mellon & Li 2008). Potential solutions that have been proposed in recent years include misalignment between the initial magnetic field and rotation axis (Joos, Hennebelle & Ciardi 2012; Li, Krasnopolsky & Shang 2013), initial turbulence (Santos-Lima, de Gouveia Dal Pino & Lazarian 2012; Seifried et al. 2013; Li et al. 2014), and non-ideal magnetohydrodynamic (MHD) effects (Tomida, Okuzumi & Machida 2015; Tsukamoto et al. 2015a, b; Masson et al. 2016; Wurster, Price & Bate 2016; Zhao et al. 2016, 2018a). For the former two candidates, however, either a large misalignment angle (Li et al. 2013) or a sonic turbulence Mach number (Li et al. 2014) is needed initially for RSDs to form and survive from dense cores magnetized to a realistic level (dimensionless mass-to-flux ratio of a few; Troland & Crutcher 2008). The large misalignment angle or turbulence level is unlikely to be the typical condition for dense cores. Kinematic studies of prestellar cores have shown that the level of turbulence in dense cores is generally sub-sonic (Fuller & Myers 1992; Caselli et al. 2002b; Keto & Caselli 2008). As dense cores are only slightly ionized (Caselli et al. 1998; Bergin & Tafalla 2007), the flux-freezing conditions in the ideal MHD limit should no longer hold during the protostellar collapse, and non-ideal MHD effects should naturally operate in dense cores.

The efficiency of the non-ideal MHD effects, especially ambipolar diffusion (AD) and Hall effect, in regulating the protostellar collapse and disc formation, depends heavily on the ionization fraction and microphysics in dense cores. Early non-ideal MHD studies on disc formation have adopted relatively low magnetic diffusivities, which lead to the general conclusion that disc formation remain suppressed (e.g. Machida, Inutsuka & Matsumoto 2007; Mellon & Li 2009; Li, Krasnopolsky & Shang 2011). In particular, AD can instead enhance the magnetic field strength and hence the magnetic braking in the inner envelope by driving a hydrodynamic C-shock that moves radially outward into the infalling flow (so-called 'AD-shock'; Li &

★ E-mail: bz6g@mpe.mpg.de
† Present address: 1280 Main Street West, Hamilton, Canada, L8S 4K1.

Published by Oxford University Press on behalf of Royal Astronomical Society

McKee 1996; Krasnopolsky & Königl 2002; Li et al. 2011). The formation of AD-shock owes to a negligible decoupling of magnetic fields in the bulk envelope and an abrupt decoupling in the stellar vicinity, which could be mostly avoided by a larger ambipolar diffusivity in the envelope (Krasnopolsky & Königl 2002; Zhao et al. 2018a). Nevertheless, the general consensus is that magnetic diffusivities in the collapsing envelope have to be enhanced by $\sim$1–2 orders of magnitude than the values adopted in these early studies, so as to enable the formation of tens-of-au RSDs (Shu et al. 2006; Krasnopolsky, Li & Shang 2010).

The main microphysical properties that control the magnetic diffusivities are cosmic ray (CR) ionization rate and grain size distribution (e.g. Padovani et al. 2014; Zhao et al. 2016). The CR ionization rate affects the overall magnitude of magnetic diffusivities (Umebayashi & Nakano 1990) while a large population of very small grains (VSGs: $\sim$1 nm to few 10 nm) can dominate the fluid conductivity (Zhao et al. 2016; Dzyurkevich et al. 2017). Dapp, Basu & Kunz (2012) combine AD and Ohmic dissipation into an effective resistivity and explore different grain sizes for the resistivity computation. Their result reveals a strong dependence of the combined resistivity on grain sizes, especially at envelope densities ($\lesssim 10^{10}$ cm^{-3}). However, the somewhat high CR ionization rate (5×10^{-17} s^{-1}) and slow initial rotation adopted in their study likely prevent the formation of sizable discs. Later, detailed investigations of the impact of grain size distribution on magnetic diffusivities have been carried out (Padovani et al. 2014; Zhao et al. 2016; Dzyurkevich et al. 2017; Koga et al. 2019), confirming the trend found in Dapp et al. (2012) that slightly increasing the average grain size can enhance the ambipolar diffusivity by $\sim$1–2 orders of magnitude in comparison to the standard Mathis-Rumpl-Nordsieck (MRN; Mathis, Rumpl & Nordsieck 1977, a -3.5 power law with size ranging from $a_{\min} \sim 0.005$ μm to $a_{\max} \sim 0.25$ μm) size distribution. As shown analytically and numerically, the smallest grains are rapidly depleted in cold dense environment (Ossenkopf 1993; Hirashita 2012; Köhler et al. 2012; Guillet et al. 2020; Silsbee et al. 2020), which is supported by the non-detection of spinning dust grain emission (produced by VSGs of $\lesssim$10 nm) in recent Galactic cold core surveys (Tibbs et al. 2016). In fact, many recent non-ideal MHD simulations of disc formation have adopted grain size distributions free of VSGs for computing the magnetic diffusivities, for example, singly sized 0.1 μm grains (Tomida et al. 2015), or a 'modified' MRN size distribution (Marchand et al. 2016; Masson et al. 2016; Hennebelle et al. 2020), both of which would enhance the ambipolar diffusivity and promote disc formation.

Hall effect has recently been discussed extensively (Krasnopolsky, Li & Shang 2011; Braiding & Wardle 2012a, b; Tsukamoto et al. 2015b; Wurster et al. 2016; Marchand et al. 2018; Zhao et al. 2020) and claimed by several studies as the dominant mechanism for enabling a bimodal disc formation (e.g. Tsukamoto et al. 2017; Wurster & Li 2018), i.e. only when the angular velocity vector ($\boldsymbol{\Omega}$) of the initial core is anti-aligned with the magnetic field ($\boldsymbol{B}$) that disc formation is possible. However, as pointed out by Zhao et al. (2020, hereafter Paper I), the bimodality of disc formation by Hall effect does not continue into the main accretion phase; and in the absence of AD, Hall effect only allows the formation of $\sim$10–20 au RSDs regardless of the sign of $\boldsymbol{\Omega} \cdot \boldsymbol{B}$. Particularly, in the aligned configuration ($\boldsymbol{\Omega} \cdot \boldsymbol{B} > 0$), both the disc and the inner envelope are counterrotating with respect to the bulk core rotation. Moreover, the Hall diffusivity also benefits from removing the smallest $\lesssim$10 nm grains from the standard MRN size distribution, but reaches a maximum level at inner envelope densities when the minimum grain size is set to $\sim$0.03–0.04 μm (Zhao, Caselli & Li 2018b; Koga et al. 2019). As shown in Paper I, disc formation is strongly suppressed in models adopting the standard MRN size distribution, which is in agreement with the result of Li et al. (2011). In contrast, the grain size distribution in recent Hall studies are in general VSG-free (e.g. Tsukamoto et al. 2015b; Wurster et al. 2016), which naturally gives rise to efficient Hall effect. In particular, the grain size of 0.035 μm adopted by Tsukamoto et al. (2015b) is very close to the average grain size needed for maximizing the Hall diffusivity, which causes Hall effect to dominate over AD in the collapsing envelope, as we will reveal in this study. Therefore, it is crucial to ensure the convergence of the microphysical properties and ionization chemistry before comparing the results of non-ideal MHD simulations of disc formation.

The work of Dzyurkevich et al. (2017), Zhao et al. (2018b), and Koga et al. (2019) have also discovered that ambipolar and Hall diffusivities behave differently when varying the grain sizes, and each diffusivity reaches its individual maximum level with a slightly different grain size ($a_{\min}$ at $\sim$0.1 μm for ambipolar but $\sim$0.03–0.04 μm for Hall). Such a difference can potentially allow AD and Hall effect to compensate each other as grain sizes change, when at least one of the two diffusivities is large enough. However, unlike AD that is diffusive along the bending direction of the magnetic field, Hall effect is a dispersive process that drifts the magnetic field lines along the orthogonal direction. Therefore, AD and Hall effect can interact in a non-trivial way depending on the relative importance of the two mechanisms. The impact of a varying ratio of Hall to ambipolar diffusivity on disc formation was first discussed by Braiding & Wardle (2012a), but only as a free parameter ranging from -0.5 to 0.2. In fact, the absolute value of Hall diffusivity can also become larger than the ambipolar diffusivity in the inner envelope when $a_{\min}$ is around 0.03–0.04 μm. In this paper, we will go beyond Paper I and elaborate on how microphysics changes the relative importance of AD and Hall effect, and on how the two effects interplay with each other during the protostellar collapse and disc formation.

The rest of the paper is organized as follows. We demonstrate in Section 2 the basic principles of non-ideal MHD effects in disc formation, and analyse in detail the ambipolar and Hall drift in the radial and azimuthal direction along the pseudo-disc; a generalized principle of the AD-Hall interplay is derived. Section 3 describes the initial conditions of the simulation set, together with an overview of the results. In Section 4, we start from the standard MRN size distribution, and demonstrate how the removal of the smallest nanometre-grain population can promote disc formation, and how further changes in microphysics can lead to either a Hall-dominated collapse or an AD-dominated collapse. We show that disc formation is greatly promoted because of the persistent outward diffusion of magnetic fields in the radial direction. In Section 5, we discuss the impact of microphysics on disc and outflow morphologies, and connect the process of disc formation to protoplanetary disc evolution. Finally, we summarize the results in Section 6.

2 NON-IDEAL MHD EFFECTS

The evolution of magnetic field $\boldsymbol{B}$ in astrophysical fluids is governed by the magnetic induction equation,

$$\begin{aligned}\frac{\partial \boldsymbol{B}}{\partial t} &= \nabla \times (\boldsymbol{v} \times \boldsymbol{B}) - \nabla \times \left\{ \eta_{\rm O} \nabla \times \boldsymbol{B} + \eta_{\rm H} (\nabla \times \boldsymbol{B}) \times \frac{\boldsymbol{B}}{B} \right.\\ &\qquad \left. + \, \eta_{\rm AD} \frac{\boldsymbol{B}}{B} \times \left[(\nabla \times \boldsymbol{B}) \times \frac{\boldsymbol{B}}{B} \right] \right\}\\ &= \nabla \times \left[(\boldsymbol{v} + \boldsymbol{v}_{\rm H} + \boldsymbol{v}_{\rm AD}) \times \boldsymbol{B} - \eta_{\rm O} \nabla \times \boldsymbol{B} \right] , \qquad (1)\end{aligned}$$

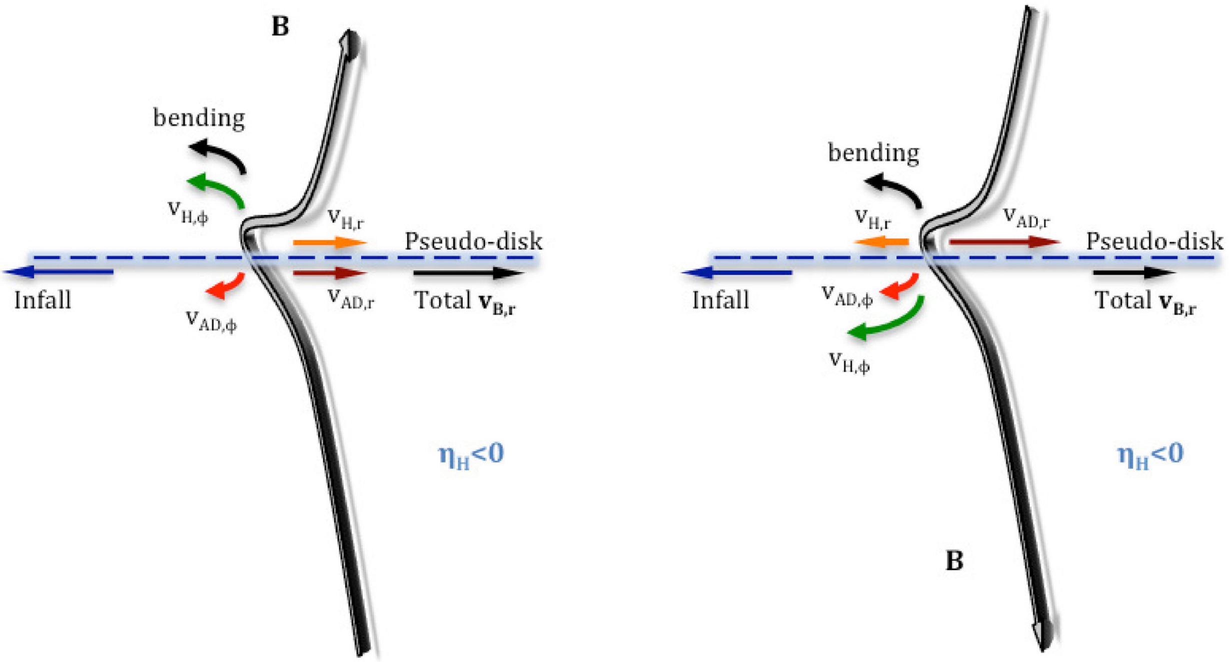

Figure 1. Illustration of the interplay between Hall and AD effect in the collapsing envelope. In the radial direction, the combined effect of AD and Hall effect is to drift the magnetic fields radially outward. For the other two cases with the magnetic field being bended azimuthally towards the reader, the conclusions are similar. Note that the same principle can be applied to the protostellar disc, where magnetic field lines are primarily bended azimuthally by rotation instead of radially by infall.

where $\boldsymbol{v}$ is the fluid velocity; $\eta_{\rm O}$, $\eta_{\rm H}$, and $\eta_{\rm AD}$ are the Ohmic, Hall, and ambipolar diffusivities, respectively; and $\boldsymbol{v}_{\rm H}$ and $\boldsymbol{v}_{\rm AD}$ denote the drift velocities of magnetic field lines induced by Hall effect and AD, respectively, which are defined as

$$\boldsymbol{v}_{\rm H} = -\eta_{\rm H}\frac{\nabla\times\boldsymbol{B}}{B} = -\eta_{\rm H}\frac{4\pi\boldsymbol{J}}{cB}\ , \tag{2}$$

$$\boldsymbol{v}_{\rm AD} = \eta_{\rm AD}\frac{(\nabla\times\boldsymbol{B})\times\boldsymbol{B}}{B^2} = \eta_{\rm AD}\frac{4\pi\boldsymbol{J}\times\boldsymbol{B}}{cB^2}\ , \tag{3}$$

where c is the light speed, and $\boldsymbol{J}$ is the electric current. In what follows, we dissect the components of these drift velocities, as to better understand the role of non-ideal MHD effects in disc formation and evolution.

2.1 Ambipolar and Hall drift

Since ambipolar diffusivity $\eta_{\rm AD}$ is always positive (Wardle & Ng 1999), the direction of ambipolar drift in general points away from the bending direction of the magnetic field (Fig. 1; see also Zhao et al. 2018a); namely, the ambipolar drift tends to relax the magnetic field bending, both radially and azimuthally, via magnetic tension force (equation 3). In the context of core collapse and disc formation, the bending of magnetic fields is the most severe along the pseudo-disc (usually the equatorial plane) or across the disc mid-plane. At such locations, the radial and azimuthal components of ambipolar drift velocity ($v_{{\rm AD},r}$ and $v_{{\rm AD},\phi}$) can be conveniently expressed in cylindrical coordinates as

$$v_{{\rm AD},r} \approx \frac{\eta_{\rm AD}B_z}{B^2}\frac{\partial B_r}{\partial z}\ , \tag{4}$$

and

$$v_{{\rm AD},\phi} \approx \frac{\eta_{\rm AD}B_z}{B^2}\frac{\partial B_\phi}{\partial z}\ , \tag{5}$$

respectively, where B_z, B_r, and B_ϕ are the poloidal, radial, and azimuthal components of the magnetic field, respectively. We keep only the leading terms, since along the pseudo-disc, the electric current in z-direction is negligible, and the gradient of poloidal magnetic field B_z in both r- and ϕ- directions, $|\frac{\partial B_z}{\partial r}|$ and $\frac{1}{r}|\frac{\partial B_z}{\partial \phi}|$, is much smaller than the changes of magnetic fields across the pseudo-disc, $|\frac{\partial B_r}{\partial z}|$ and $|\frac{\partial B_\phi}{\partial z}|$ (see also Zhao et al. 2018a). It is clear that the ambipolar drift velocity is primarily determined by the magnetic field bending in the corresponding direction, i.e. $v_{{\rm AD},r} \propto \frac{\partial B_r}{\partial z}$ and $v_{{\rm AD},\phi} \propto \frac{\partial B_\phi}{\partial z}$. In particular, when the poloidal magnetic field lines are preferentially pinched inward, the radial ambipolar drift always points radially outward ($B_z\frac{\partial B_r}{\partial z} > 0$ in equation 4).

In comparison, the Hall drift in a given direction is induced by the magnetic field bending in the orthogonal direction. As we have demonstrated in Paper I, the radial and azimuthal components of the Hall drift velocity ($v_{{\rm H},r}$ and $v_{{\rm H},\phi}$) along the pseudo-disc or across the disc mid-plane can be estimated, keeping only the leading terms (similar to the AD case above), as

$$v_{{\rm H},r} \approx \frac{\eta_{\rm H}}{B}\frac{\partial B_\phi}{\partial z}\ , \tag{6}$$

and

$$v_{{\rm H},\phi} \approx -\frac{\eta_{\rm H}}{B}\frac{\partial B_r}{\partial z}\ , \tag{7}$$

respectively (see also Bai & Stone 2017 and Paper I for more detailed discussion). Basically, the Hall drift velocities are related to the magnetic field bending as $v_{{\rm H},r} \propto \frac{\partial B_\phi}{\partial z}$ and $v_{{\rm H},\phi} \propto \frac{\partial B_r}{\partial z}$. Note that Hall drift originates from the drift between positively and negatively charged species, thus $\eta_{\rm H}$ can be either positive (e.g. electrons drift relative to ions or positively charged grains) or negative (e.g. ions drift relative to negatively charged grains).

2.2 Interplay between non-ideal MHD effects

In the envelope of a collapsing core, both the ambipolar and Hall drift affect the evolution of magnetic fields, yet at slightly different scales. In general, AD can operate efficiently throughout most of the envelope (Masson et al. 2016; Zhao et al. 2016, 2018a), while Hall effect only becomes efficient in the inner envelope (within a few 100 au; Tsukamoto et al. 2017, Paper I). The combined effect of AD and Hall can be represented by an effective drift velocity of the magnetic field lines with respect to the neutrals,

$$\boldsymbol{v}_{\rm d} = \boldsymbol{v}_{\rm AD} + \boldsymbol{v}_{\rm H}\ . \tag{8}$$

We define an effective velocity of the magnetic field lines $\boldsymbol{v}_{\rm B,eff}$ as

$$\boldsymbol{v}_{\rm B,eff} = \boldsymbol{v} + \boldsymbol{v}_{\rm d}\ , \tag{9}$$

which can be substituted into equations (1) to simplify the form of the induction equation.

Along the pseudo-disc plane, where the drift velocities induced by the magnetic field bending are the largest in the envelope, the r- and ϕ- components of $\boldsymbol{v}_{\rm d}$ can be expanded, using equations (4)–(7), as

$$v_{{\rm d},r} = v_{{\rm H},r} + v_{{\rm AD},r} \approx \frac{\eta_{\rm H}}{B}\frac{\partial B_\phi}{\partial z} + \frac{\eta_{\rm AD} B_z}{B^2}\frac{\partial B_r}{\partial z}\ , \tag{10}$$

and

$$v_{{\rm d},\phi} = v_{{\rm H},\phi} + v_{{\rm AD},\phi} \approx -\frac{\eta_{\rm H}}{B}\frac{\partial B_r}{\partial z} + \frac{\eta_{\rm AD} B_z}{B^2}\frac{\partial B_\phi}{\partial z}\ , \tag{11}$$

respectively. The individual terms on the right-hand-side of equations (10)–(11) can be either positive or negative, depending on the bending direction of the magnetic field. Hence, the ambipolar and Hall drift along the pseudo-disc plane can work either *cooperatively* or *counteractively* in drifting the magnetic field in the azimuthal and radial directions. To determine the net direction of magnetic field drift in the collapsing envelope, we can utilize the fact that the poloidal magnetic field lines are preferentially pinched radially inward, and derive the possible scenarios as listed below (see illustrations in Fig. 1).

For the radial drift $v_{{\rm d},r}$, the combined effect of AD and Hall effect is to drift the magnetic field radially outward along the pseudo-disc plane, in either of the two following scenarios.

(i) (Cooperative) If the magnetic field lines are bended azimuthally (across the pseudo-disc mid-plane) towards the *same* direction as the azimuthal Hall drift $\boldsymbol{v}_{{\rm H},\phi}$, the induced radial Hall drift $\boldsymbol{v}_{{\rm H},r}$ is always along $+r$ (radially outward). In this case, both the ambipolar and Hall drift cooperatively diffuse the magnetic field radially outward (see left-hand panel of Fig. 1).

(ii) (Counteractive) If the azimuthal bending of magnetic field lines goes in the *opposite* direction of the azimuthal Hall drift $\boldsymbol{v}_{{\rm H},\phi}$, the induced radial Hall drift $\boldsymbol{v}_{{\rm H},r}$ points radially inward along $-r$ (see right-hand panel of Fig. 1). Such a configuration normally occurs in the innermost envelope where gas rotation becomes large enough to bend the magnetic field azimuthally in its direction. However, the outward ambipolar drift generally dominates such an inward Hall drift, so that the total radial drift still points outward. Basically, the following condition (equation 12) is satisfied in the innermost envelope, as the magnetic field lines are severely pinched radially but much less so azimuthally ($\frac{\partial B_r}{\partial z} \gg \frac{\partial B_\phi}{\partial z}$). Assuming a characteristic scale height of variation of magnetic field across the pseudo-disc along the z-direction, $v_{{\rm d},r} > 0$ is approximately equivalent to

$$|B_r| > \frac{|\eta_{\rm H}|}{\eta_{\rm AD}}|B_\phi|\ , \tag{12}$$

in which the ratio $\frac{|\eta_{\rm H}|}{\eta_{\rm AD}}$ is around unity in the innermost envelope, depending on the microphysics, especially the grain size distribution.

The azimuthal drift $v_{{\rm d},\phi}$ of magnetic fields is usually dominated by the Hall component $v_{{\rm H},\phi}$, because the azimuthal bending of magnetic fields that determines $v_{{\rm AD},\phi}$ is only minor in the envelope. Since the ambipolar drift $v_{{\rm AD},\phi}$ always points away from the direction of azimuthal magnetic field bending, we can obtain the following two scenarios for the azimuthal drift.

(i) (Cooperative) If the magnetic field lines are bended azimuthally in the *opposite* direction to the azimuthal Hall drift, both the ambipolar and Hall drift, $v_{{\rm AD},\phi}$ and $v_{{\rm H},\phi}$, cooperatively weaken the magnetic field bending in the azimuthal direction (see right-hand panel of Fig. 1).

(ii) (Counteractive) If the magnetic field lines are bended azimuthally in the *same* direction as the azimuthal Hall drift, ambipolar and Hall drift compete with each other (see left-hand panel of Fig. 1). Usually $v_{{\rm H},\phi} \gg v_{{\rm AD},\phi}$ is satisfied in the envelope, i.e. the azimuthal Hall drift dominates the total azimuthal drift $v_{{\rm d},\phi}$. However, if AD in the envelope is already efficient in relaxing the radial pinching of magnetic fields (reducing $|\frac{\partial Br}{\partial z}|$), the azimuthal Hall drift $v_{{\rm H},\phi}$ can be reduced to be comparable to $v_{{\rm AD},\phi}$; in cases where the magnetic field is weak, the direction of the total azimuthal drift can instead be determined by the azimuthal ambipolar drift that slightly weakens the azimuthal bending of magnetic fields.

It is worth noting that, if the ambipolar and Hall drift are cooperative in diffusing the magnetic field in one direction, they are counteractive in the orthogonal direction. Such a principle is directly implied from equations (10)–(11), as

$$v_{{\rm H},r}\ v_{{\rm AD},r} \approx -v_{{\rm H},\phi}\ v_{{\rm AD},\phi} \approx \frac{\eta_{\rm H}\eta_{\rm AD} B_z}{B^3}\frac{\partial B_\phi}{\partial z}\frac{\partial B_r}{\partial z}\ . \tag{13}$$

Basically, as ambipolar drift always tends to relax the field bending, the Hall drift component that operates against the ambipolar drift in one direction is constrained by a negative feedback (see also Paper I) from the Hall drift operating together with the ambipolar drift in the orthogonal direction. In other words, the cooperative drift weakens the magnetic field bending in that direction, which in turn reduces the Hall drift competing with the ambipolar drift in the orthogonal direction.

The above analysis is not limited to the collapsing envelope, but can be applied to the protostellar (or protoplanetary) disc itself. The main difference is that magnetic field lines threading the disc are primarily bended azimuthally by gas rotation, while the radial pinching is less prominent across the disc mid-plane. Thus for the disc case, in analogy to the reasoning of the envelope case, the combined effect of ambipolar and Hall drift in the azimuthal direction is to straighten the azimuthal bending of magnetic fields. In the radial direction, Hall drift usually dominates the total radial drift in most cases because of the relatively severe azimuthal bending of magnetic fields. However, if Ohmic dissipation is already efficient within the disc, the degree of magnetic field bending may become much less severe and hence both ambipolar and Hall drift can be limited (see also Paper I). Nonetheless, as the magnetic field geometry becomes more complicated in the presence of different types of instabilities in protoplanetary discs (e.g. Gressel et al. 2015; Bai & Stone 2017; Béthune, Lesur & Ferreira 2017; Suriano et al. 2018), the basic principles here may still help understand the local behaviour of magnetic fields. In what follows, we mainly focus on the behaviour of magnetic fields in the collapsing envelope, which is the key to the formation and early evolution of protostellar discs.

3 SIMULATION SET-UP

To investigate the interplay of non-ideal MHD effects in a collapsing dense core, as well as their impact on disc formation and evolution, we follow the same numerical set-up of Paper I and carry out two-dimensional (2D) axisymmetric simulations using ZEUSTW code (Krasnopolsky et al. 2010). The three non-ideal MHD effects (AD, Hall effect, and Ohmic dissipation) are included, with magnetic diffusivities obtained by linearly interpolating the tabulated equilibrium chemical network (Zhao et al. 2018b, see also Appendix. A).

The set of equations solved numerically to evolve the hydrodynamics include equations of mass and momentum conservation, magnetic induction equation (equation 1), and the Poisson equation for self-gravity. We do not directly solve the energy equation, but instead adopt a piecewise barotropic equation of state (EOS; same as that used in Zhao et al. 2018a), which is a functional fitting for the radiative transfer calculations of Tomida et al. (2013). The EOS approximately follows power laws with adiabatic index $\Gamma \sim 1.6$ and $\sim$1.44, for mass densities below and above 10^{-11} g cm^{-3}, respectively.

The initial conditions are the same as Paper I. We briefly summarize the relevant parameters. The initial core is spherically shaped, with total mass $M_c = 1.0$ M$_\odot$ and radius $R_c = 10^{17}$ cm $\approx$6684 au that corresponds to a uniform density of $\rho_0 = 4.77 \times 10^{-19}$ g cm^{-3}. The core is rotating initially as a solid-body with angular speed $\omega_0 = 1 \times 10^{-13}$ s^{-1} that corresponds to a ratio of rotational to gravitational energy $\beta_{\rm rot} \approx 0.025$ (the typical value from Goodman et al. 1993). The initial magnetic field is either aligned or anti-aligned with the angular angular velocity vector ($\boldsymbol{\Omega}$), with a uniform field strength B_0 of 42.5 μG for strong field case, 21.3 μG for weak field case, and 10.6 μG for very weak field case, which gives a dimensionless mass-to-flux λ ($\equiv \frac{M_c}{\pi R_c^2 B_0} 2\pi\sqrt{G}$) of 2.4, 4.8, and 9.6, respectively. We adopt a spherical coordinate system (r, θ, ϕ) with non-uniform grid spacing along r- and θ- directions. The smallest cell size is set to $\delta r = 0.2$ au for cells next to the inner boundary $r_{\rm in} = 2$ au. The r-direction spacing increases geometrically outward by a constant factor of $\sim$1.0663, and the θ-direction spacing increases geometrically from the equator to either pole by a constant factor of $\sim$1.0387. Note that the direction of initial rotation is along $+\phi$.

As in Paper I, the magnetic diffusivities are computed using the tabulated fractional abundances of charged species from Zhao et al. (2018b). We explore different cosmic ray (CR) ionization rates of $\zeta_0^{\rm H_2} = 10^{-17}$ s^{-1} and 10^{-16} s^{-1} at the cloud edge with a characteristic attenuation length of $\sim$200 g cm^{-2} (Padovani et al. 2018). We use 20 size bins to model the Mathis-Rumpl-Nordsieck (MRN) (Mathis et al. 1977) grain size distribution, fixing the power law index at -3.5 and the maximum grain size at $a_{\rm max} = 0.25$ μm, but varying the minimum grain size $a_{\rm min} = 0.005$, 0.03, and 0.1 μm, for MRN, opt3 (optimal for Hall effect), and trMRN (optimal for AD) models, respectively (see notes of Table 1).

To avoid intolerably small time-steps, we impose relatively small dt floors for AD and Hall effect, with d$t_{\rm floor,\,AD} = 1 \times 10^5$ s and d$t_{\rm floor,\,H} = 3 \times 10^4$ s, which cap the ambipolar and Hall diffusivities.[1] Similar to Paper I, we place a resistivity floor for Ohmic dissipation, which equals to the smaller of 10^{18} cm^2 s^{-1} and $\eta_{\rm H}$, to ensure the stability of the Hall solver but to not noticeably weaken the electric current density in the inner envelope (Krasnopolsky et al. 2011). Note that the Ohmic diffusivity in the disc is mostly above 10^{20} cm^2 s^{-1} (well above the resistivity floor), which is large enough to limit the radial (B_r) and azimuthal (B_ϕ) components of the magnetic field as well as the corresponding AD and Hall effect in the disc.

We summarize a total of 32 numerical models in Tables 1–3, surveying the parameter space of magnetic field strength and direction, grain size distribution, and CR ionization rate.

Table 1. Model parameters for strong B-field $B_0 \approx 42.5$ μG ($\lambda \sim 2.4$).

Model‡	Grain Size† Dist.	$\zeta_0^{\rm H_2}$ (10^{-17} s^{-1})	$\beta_{\rm rot}$	Radius & Morphology* (au)
2.4MRN_AH$^-$O	MRN	1	0.025	<2
2.4MRN_AH$^+$O	MRN	1	0.025	<2
2.4min1_AH$^-$O	min1	1	0.025	$\sim$20 (Disc + Spiral/Ring)
2.4min1_AH$^+$O	min1	1	0.025	$\downarrow <2 \Rightarrow \lesssim 20^{\circlearrowleft}$
2.4opt3_AH$^-$O	opt3	1	0.025	20–30 (Disc + Spiral/Ring)
2.4opt3_AH$^+$O	opt3	1	0.025	$\downarrow <2 \Rightarrow \sim 30^{\circlearrowleft}$
2.4$_{\rm Slw}$opt3_AH$^-$O	opt3	1	6.25×10^{-3}	$\lesssim$30
2.4$_{\rm Slw}$opt3_AH$^+$O	opt3	1	6.25×10^{-3}	$\downarrow <2 \Rightarrow \sim 30^{\circlearrowleft}$
2.4$_{\rm NoRot}$opt3_AHO	opt3	1	0	$\sim 30^{\circlearrowleft}$
2.4trMRN_AO	trMRN	1	0.025	$\lesssim$20 (Disc + Spiral/Ring)
2.4trMRN_AH$^-$O	trMRN	1	0.025	$\sim$20 (Disc + Spiral/Ring)
2.4trMRN_AH$^+$O	trMRN	1	0.025	$\lesssim$20 (Disc + Spiral/Ring)
2.4$_{\rm NoRot}$trMRN_AHO	trMRN	1	0	—
2.4CR10opt3_AH$^-$O	opt3	10	0.025	$\lesssim$10
2.4CR10opt3_AH$^+$O	opt3	10	0.025	$\downarrow <2 \Rightarrow \sim 10^{\circlearrowleft}$
2.4CR50opt2_AH$^-$O	opt2	50	0.025	<2
2.4CR50opt2_AH$^+$O	opt2	50	0.025	<2

Notes. †MRN: full MRN distribution with $a_{\rm min} = 0.005$ μm
†min1: truncated MRN distribution with $a_{\rm min} = 0.01$ μm
†opt3: truncated MRN distribution with $a_{\rm min} = 0.03$ μm, with which Hall diffusivity reaches an optimal level in the inner envelope
†trMRN: truncated MRN distribution with $a_{\rm min} = 0.1$ μm
†LG: singly sized grains with $a = 1.0$ μm; note that LG models have $\eta_{\rm H} > 0$ at the envelope scale, the opposite to other size distributions
‡AH$^-$O: AD+Hall + Ohmic model with anti-aligned configuration ($\boldsymbol{\Omega} \cdot \boldsymbol{B} < 0$)
‡AH$^+$O: AD+Hall + Ohmic model with aligned configuration ($\boldsymbol{\Omega} \cdot \boldsymbol{B} > 0$)
‡AO: AD + Ohmic model
‡$_{\rm Slw}$: model with slow initial core rotation
‡$_{\rm NoRot}$: model with zero initial core rotation
∗The ↑ or ↓ symbol indicates that the disc radius is growing or shrinking, repectively
∗The $^{\circlearrowleft}$ symbol indicates that the disc is counterrotating with respect to the initial core rotation

Table 2. Model parameters for weak B-field $B_0 \approx 21.3$ μG ($\lambda \sim 4.8$).

Model	Grain size Dist.	$\zeta_0^{\rm H_2}$ (10^{-17} s^{-1})	$\beta_{\rm rot}$	Radius and morphology (au)
4.8MRN_AH$^-$O	MRN	1	0.025	$\sim 13\!\downarrow <2$
4.8MRN_AH$^+$O	MRN	1	0.025	$\sim 12\!\downarrow <2$
4.8min1_AH$^-$O	min1	1	0.025	$\sim$25 (Disc + Spiral/Ring)
4.8min1_AH$^+$O	min1	1	0.025	$\downarrow <2 \Rightarrow \lesssim 23^{\circlearrowleft}$
4.8opt3_AH$^-$O	opt3	1	0.025	20–30 (Disc + Spiral/Ring)
4.8opt3_AH$^+$O	opt3	1	0.025	$\sim 15\!\downarrow <2 \Rightarrow \lesssim 20^{\circlearrowleft}$
4.8$_{\rm Slw}$opt3_AH$^-$O	opt3	1	6.25×10^{-3}	$\lesssim$30
4.8$_{\rm Slw}$opt3_AH$^+$O	opt3	1	6.25×10^{-3}	$\downarrow <2 \Rightarrow \lesssim 20^{\circlearrowleft}$
4.8$_{\rm NoRot}$opt3_AHO	opt3	1	0	$\sim 35^{\circlearrowleft}$
4.8trMRN_AO	trMRN	1	0.025	$\lesssim$30 (Disc + Spiral/Ring)
4.8trMRN_AH$^-$O	trMRN	1	0.025	$\sim$30 (Disc + Spiral/Ring)
4.8trMRN_AH$^+$O	trMRN	1	0.025	$\lesssim$30 (Disc + Spiral/Ring)
4.8$_{\rm NoRot}$trMRN_AHO	trMRN	1	0	—
4.8CR10opt3_AH$^-$O	opt3	10	0.025	$\sim 16\!\downarrow \sim 10$
4.8CR10opt3_AH$^+$O	opt3	10	0.025	$\sim 12\!\downarrow <2 \Rightarrow \sim 12^{\circlearrowleft}$
4.8CR50opt2_AH$^-$O	opt2	50	0.025	$\lesssim 10\!\downarrow <2$
4.8CR50opt2_AH$^+$O	opt2	50	0.025	$\lesssim 8\!\downarrow <2$

Table 3. Model parameters for very weak B-field $B_0 \approx 10.6$ μG ($\lambda \sim 9.6$).

Model	Grain size Dist.	$\zeta_0^{\rm H_2}$ (10^{-17} s^{-1})	$\beta_{\rm rot}$	Radius and morphology (au)
9.6opt3_AH$^-$O	opt3	1	0.025	20–30 (Disc + Spiral/Ring)
9.6opt3_AH$^+$O	opt3	1	0.025	$\sim$40 (Disc + Spiral/Ring)
9.6opt3_AHO	opt3	1	0	—

---

[1] The cap of $\eta_{\rm AD}$ and $\eta_{\rm H}$ is computed for each cell as CFL$\frac{|\delta x|^2_{\rm min}}{4{\rm d}t_{\rm floor}}$, where CFL is the Courant–Friedrich–Lewy number that is set to 0.4 for AD and 0.2 for Hall, and $|\delta x|_{\rm min}$ is the smallest of the cell's sizes along r and θ directions.

4 SIMULATION RESULTS

As shown in Tables 1–3, disc formation is sensitive to both the grain size distribution and the CR ionization rate. A high $\zeta_0^{\mathrm{H_2}}$ (at the core scale) close to 5×10^{-16} s^{-1}, or the inclusion of the large population of VSGs (e.g. MRN models) strongly suppresses the formation of sizable RSDs larger than the $\sim$2 au inner boundary. Similar to Paper I, the polarity of the magnetic field does not determine whether discs form or not, but can affect the direction of disc rotation in relatively strongly magnetized cores ($\lambda \lesssim 5$). However, in comparison to Paper I (with no AD), counterrotating discs only appear in the aligned ($\boldsymbol{\Omega} \cdot \boldsymbol{B} > 0$) models with relatively small $a_{\min}$, but not in the aligned models with $a_{\min}$ increased to $\sim$0.1 µm (or above); it is a phenomenon controlled by the relative magnitude of η_{AD} and η_{H}, and will be discussed in details in Sections 4.2 and 4.3.

Note that the disc radii are of the order of 20–30 au in models with the canonical CR ionization rate of 10^{-17} s^{-1}; many of these discs or their extended spiral structures tend to grow further at later times, which can be better demonstrated in 3D studies. In contrast, the disc radii in models with high CR ionization rate ($\gtrsim 10^{-16}$ s^{-1}) remain at $\lesssim$10 au throughout their evolution.

4.1 Suppression of disc formation by VSGs

When the standard MRN size distribution is adopted, in which the highly conductive VSG population is suppressing the magnetic diffusivities in the collapsing envelope (Zhao et al. 2016, 2018b; Dzyurkevich et al. 2017), including all three non-ideal MHD effects does not save disc formation, which is in agreement with the result of Li et al. (2011). As shown in Fig. 2, the results from the anti-aligned model 2.4MRN_AH^{-}O and the aligned model 2.4MRN_AH^{+}O are nearly identical, i.e. both show no obvious RSDs larger than r_{in} (2 au) throughout the protostellar collapse and accretion phase. The main difference is the rotation direction of the inner accreting flow ($\lesssim$100 au) around the central object, which is the same as the envelope rotation in the anti-aligned case, while the opposite to the envelope rotation in the aligned case. However, the rotation speed v_ϕ in both cases are well below the Keplerian speed, consistent with the lack of rotationally supported structures in the density distribution.

The absence of RSDs in the MRN models is a result of the insufficient drift of magnetic fields in the bulk envelope. The drift velocity $\boldsymbol{v}_{\mathrm{d}}$ can be estimated in Fig. 2 by the difference between the effective velocity of the magnetic field lines $\boldsymbol{v}_{\mathrm{B,eff}}$ and the bulk neutral velocity $\boldsymbol{v}$. For convenience of analysis, we also define an effective velocity of the magnetic field lines due to Hall drift alone (see also Paper I), as

$$\boldsymbol{v}_{\mathrm{BH}} = \boldsymbol{v} + \boldsymbol{v}_{\mathrm{H}}\ . \qquad (14)$$

In either model, the azimuthal drift of magnetic fields is primarily dominated by the azimuthal Hall drift: $v_{\mathrm{B,eff},\phi} \approx v_{\mathrm{BH},\phi}$, while the radial drift of magnetic fields is almost entirely determined by the radial ambipolar drift: $|v_{\mathrm{B,eff},r}| \ll |v_r| \approx |v_{\mathrm{BH},r}|$. However, the radial ambipolar drift only becomes prominent in the inner $\lesssim$100 au, but is nearly vanishing in the outer part of the collapsing envelope. In other words, the amount of magnetic flux being dragged into the inner $\lesssim$100 au region is not much different from the ideal MHD limit. As already shown in previous studies (Li et al. 2011; Zhao et al. 2018a; Lam et al. 2019), radial diffusion of magnetic fields only within the inner $\lesssim$100 au by AD is unable to save disc formation;[2] either additional radial diffusion in the bulk envelope (limiting the magnetic flux arrived in the inner envelope; Zhao et al. 2018a) and/or efficient azimuthal diffusion by Hall effect (limiting the radial current $J_r \propto \frac{\partial B_\phi}{\partial z}$; see also Paper I) are needed for weakening the magnetic braking torque, which are unfortunately not achieved with the standard MRN size distribution. More specifically (Fig. 3), the ambipolar diffusivity η_{AD} along the pseudo-disc (equatorial plane) is of the order of $\sim 10^{17}$ cm^2 s^{-1} at 10^2–10^3 au scale, while the Hall diffusivity η_{H} along the pseudo-disc remains at a few 10^{17} cm^2 s^{-1} in the inner $\lesssim$100 au. Such values of diffusivities in the inner envelope are 1–2 orders of magnitude below the required level for disc formation suggested by Shu et al. (2006) and Krasnopolsky et al. (2010). Note that in the inner envelope, η_{AD} only increases above 10^{18} cm^2 s^{-1} (a few times larger than η_{H}) within the $\lesssim$100 au region where ambipolar drift becomes prominent.

4.2 Hall-dominated collapse: bimodal disc rotation

As we slightly increase $a_{\min}$, i.e. truncating off the large population of VSGs ($\lesssim$10 nm) from the grain size distribution, disc formation becomes insensitive to further changes in grain sizes. We first focus on the models adopting $a_{\min} = 0.03$ µm, with which the Hall diffusivity η_{H} reaches an optimal level throughout the collapsing envelope (Zhao et al. 2018b; Koga et al. 2019), while the ambipolar diffusivity η_{AD} has not yet reached its optimal level (Zhao et al. 2016). We show that in such models AD and Hall effect operate together to promote disc formation. In particular, Hall effect efficiently regulates the magnetic field drift and gas dynamics in the inner envelope, causing the discs to rotate in opposite directions depending on the polarity of the magnetic field at the core scale.

4.2.1 Anti-aligned case $\boldsymbol{\Omega} \cdot \boldsymbol{B} < 0$

Fig. 4 shows the evolution of the inner $\sim$70 au of the anti-aligned model 2.4opt3_AH^{-}O, in which an RSD forms after the first core (Larson 1969) stage and grows in radius within $\sim$5 kyr to $\sim$30 au. The disc formation and growth is a result of the combined effort of AD and Hall effect in weakening the magnetic braking torque or exerting a spin-up torque. In the azimuthal direction, the magnetic field is predominantly drifted towards $-\phi$ along the pseudo-disc by Hall effect ($v_{\mathrm{BH},\phi} \approx v_{\mathrm{B,eff},\phi}$), like in the MRN models but with a more substantial Hall drift velocity $v_{\mathrm{H},\phi}$. Similar to Paper I, $v_{\mathrm{H},\phi}$ here is large enough to overbend the magnetic field lines towards $-\phi$-direction (e.g. Fig. 5), causing a spin-up torque to accelerate the gas rotation along $+\phi$-direction in the inner envelope. In the radial direction, both AD and Hall effect contribute to the magnetic field drift, with the total drift $v_{\mathrm{d},r}$ almost always pointing towards $+r$ (radially outward) in the inner envelope (from the disc edge up to $\lesssim 10^3$ au). The persistent outward diffusion of magnetic fields decreases the amount of magnetic flux that would otherwise be dragged into the innermost region (reducing B_z). Hence, even as the azimuthal bending of magnetic fields is flipped back to $+\phi$-direction in the innermost region by the large gas rotation (along $+\phi$), the resulting spin-down (magnetic braking) torque is weakened due to the reduced poloidal magnetic field (B_z).

---

[2] Note that the inner $\lesssim$100 au, where $v_{\mathrm{B,eff},r}$ drops below 0.5 km s^{-1} due to ambipolar drift ($v_{\mathrm{AD},r} \sim$ a few km s^{-1}), corresponds to the so-called 'diffusion DEMS' (Decoupling-Enabled Magnetic Structures) demonstrated in Lam et al. (2019) or the AD-induced magnetic plateau found by Masson et al. (2016). The existence of such structures is a natural diffusive response of the magnetic field, instead of a prerequisite for the formation of sizable RSDs.

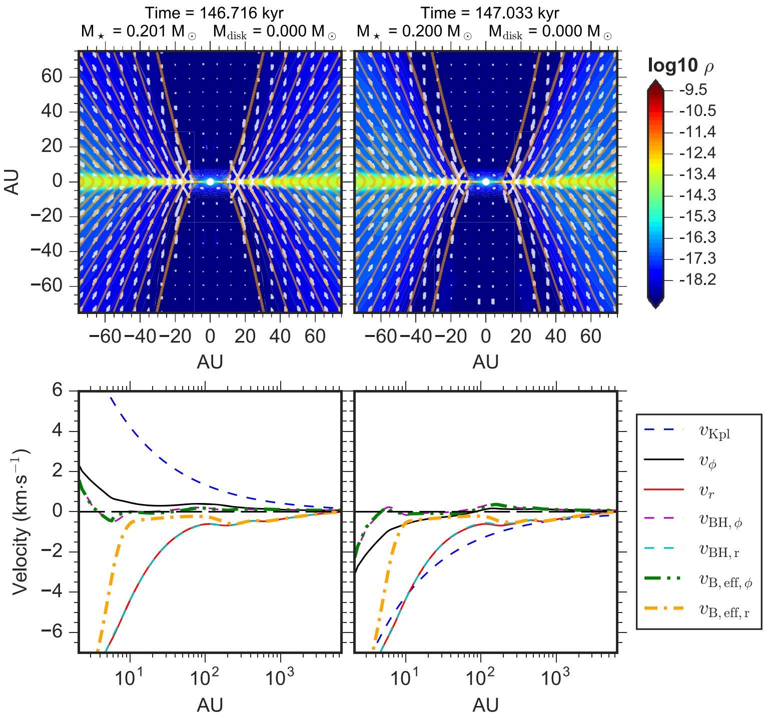

(a) Anti-aligned: $\boldsymbol{\Omega}\cdot\boldsymbol{B} < 0$ (b) Aligned: $\boldsymbol{\Omega}\cdot\boldsymbol{B} > 0$

Figure 2. Mass density distribution (top) and velocity profile along the equator (bottom) for model 2.4MRN_AH$^-$O (left-hand panels) and model 2.4MRN_AH$^+$O (right-hand panels). The white arrows and orange lines in the top panel are the velocity field vectors and magnetic field lines, respectively.

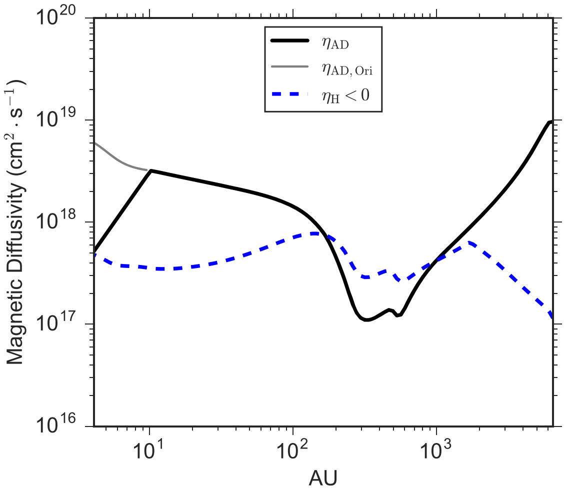

Figure 3. Radial profile of the magnetic diffusivities along the equator for the 2.4MRN_AH$^-$O model at 146.716 kyr. The grey solid line of $\eta_{\rm AD,\,Ori}$ implies the original ambipolar diffusivity unaffected by the AD dt floor. Note that $\eta_{\rm H}$ is low enough in the MRN models that Hall dt floor is not triggered.

Although the net effect of AD and Hall effect in the radial direction is to move the magnetic field radially outward relative to the infalling matter, the two effects can either be cooperative or counteractive, depending on the direction of azimuthal bending of magnetic fields. For example, at $t = 138.160$ kyr (middle panels of Fig. 4), the radial Hall drift velocity $v_{{\rm H},r}$ is positive ($v_{{\rm BH},r} - v_r > 0$) in the range ∼40–400 au, i.e. pointing towards $+r$, which is the same as the direction of the radial ambipolar drift $v_{{\rm AD},r}$ (as $v_{{\rm B,eff},r} - v_{{\rm BH},r} > 0$); in this case, the radial ambipolar and Hall drift velocities are cooperatively diffusing the magnetic field outward. However, in the range ∼27–40 au, as the large gas rotation reverses the azimuthal bending of magnetic fields to $+\phi$ (Fig. 5), the radial Hall drift $v_{{\rm H},r}$ flips its sign to negative, i.e. pointing towards $-r$, which is the opposite of the radial ambipolar drift $v_{{\rm AD},r}$. In spite of such a counteractive effect, $v_{{\rm AD},r}$ is much larger than $v_{{\rm H},r}$ (see equations 12 in Section 2.2), so that the total radial drift still points towards $+r$ (as $v_{{\rm d},r} > 0$). Such an interplay between the radial AD and Hall drift is even more prominent at later times (e.g. $t = 142.280$ kyr).

In comparison to the MRN model (2.4MRN_AH$^-$O) above, the elevated role of AD and Hall effect in the collapsing envelope of the opt3 model (2.4opt3_AH$^-$O) is primarily caused by the enhanced level of the ambipolar ($\eta_{\rm AD}$) and Hall ($\eta_{\rm H}$) diffusivities. Comparing Fig. 6 with Fig. 3, the ambipolar diffusivity $\eta_{\rm AD}$ beyond 200 au scale differs by $\gtrsim$1 order of magnitude, with the opt3 model having the larger $\eta_{\rm AD}$ (∼10^{18}–10^{20} cm^2 s^{-1} versus ∼10^{17}–10^{19} cm^2 s^{-1} in the MRN model). As a result, the ambipolar drift in the opt3 model already becomes visible at the envelope scale in the range 200–800 au ($v_{{\rm AD},r} \gtrsim 0.1$ km s^{-1}), as compared to the vanishing $v_{{\rm AD},r}$ in the MRN model. The Hall diffusivity $\eta_{\rm H}$ in the opt3 model is also larger by ∼1 order of magnitude than in the MRN model, especially within the inner $\lesssim$100–200 au where Hall effect becomes pronounced in regulating the magnetic field and gas dynamics (Tsukamoto et al. 2017, Paper I). In fact, in the range ∼40–200 au of the opt3 model, $\eta_{\rm H}$ is dominating over $\eta_{\rm AD}$ by a factor of a few along the equatorial region.

Under the efficient AD and Hall effect, the RSD formed in the 2.4opt3_AH$^-$O model survives throughout the simulated protostellar

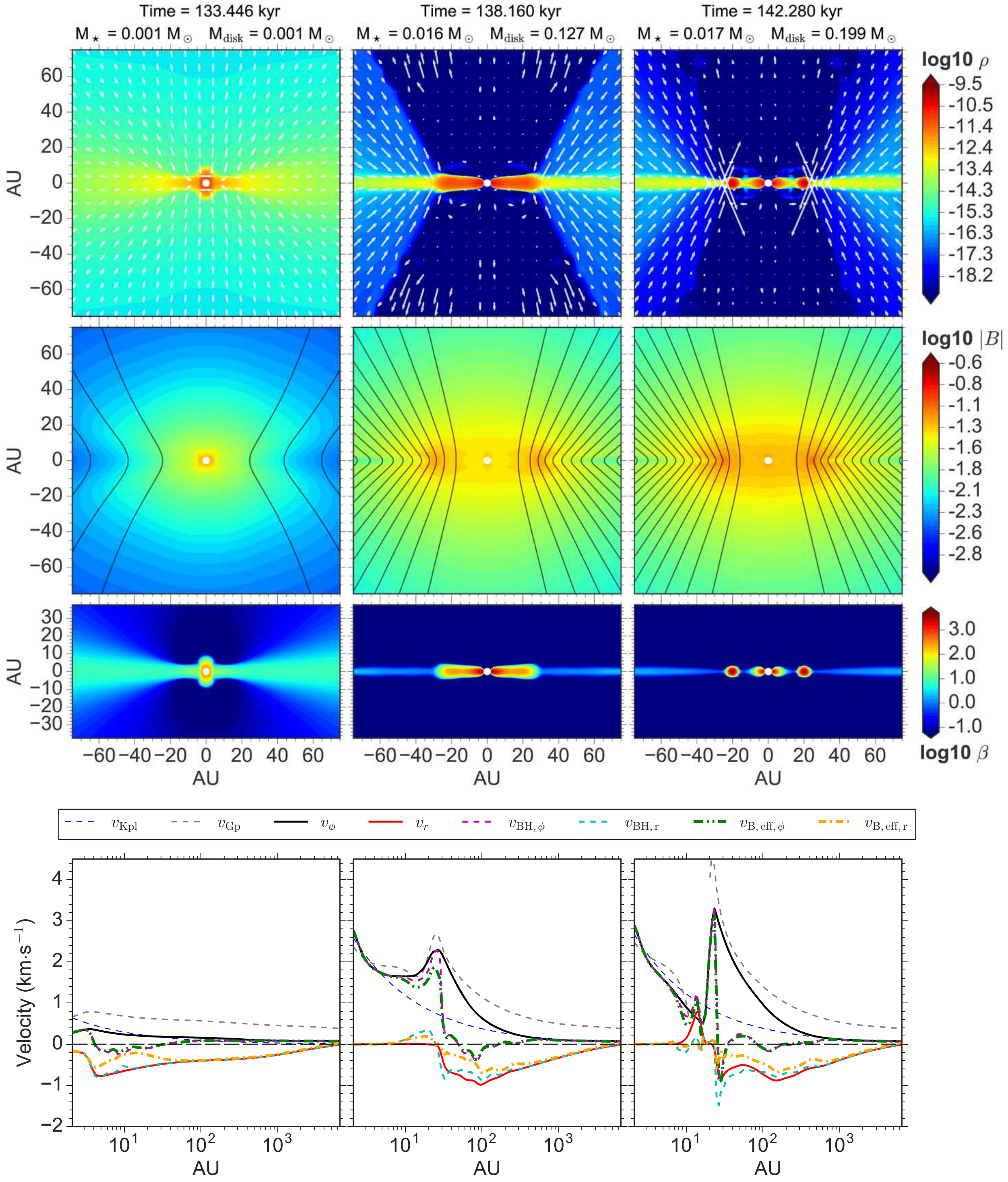

Figure 4. Evolution of disc in the anti-aligned model 2.4opt3_H$^-$O. First row: logarithmic distribution of mass density along with velocity field vectors (white arrows). Second row: logarithmic distribution of total magnetic field strength $|B|$ along with magnetic field lines (black solid lines). Third row: logarithmic distribution of plasma-β. Fourth row: velocity profile along the equator. The abrupt change of infall speed v_r near the disc edge or ring structure corresponds to the location of the centrifugal shock.

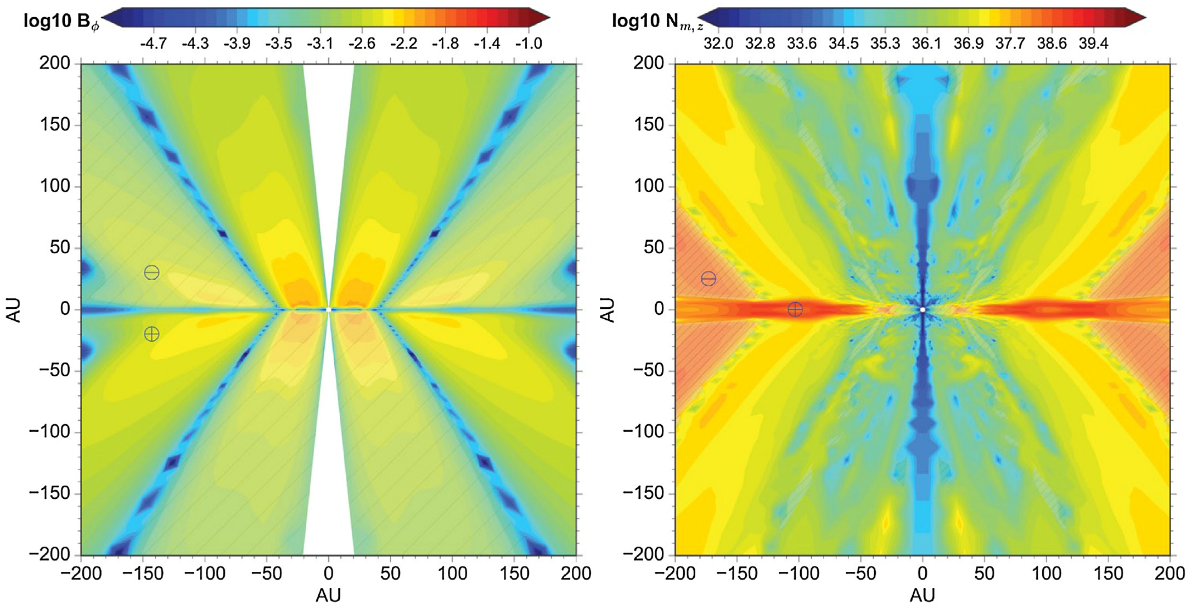

Figure 5. Logarithmic distribution of azimuthal magnetic field B_ϕ (left-hand panel) and magnetic torque $N_{\mathrm{m},\,z}$ (right-hand panel) at $t = 138.160$ kyr of the anti-aligned model 2.4opt3_AH$^-$O. B_ϕ is positive (along $+\phi$) in the unshaded region and negative (along $-\phi$) in the shaded region. Similarly, regions of negative magnetic torque (along $-z$) are shown as shaded.

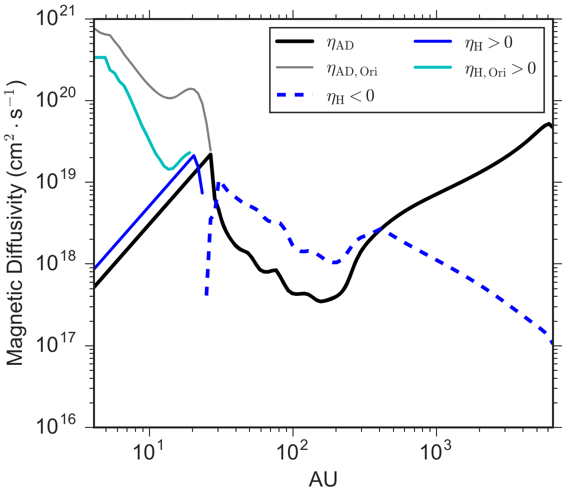

Figure 6. Radial profile of the magnetic diffusivities along the equator for the 2.4opt3_AH$^-$O model at 138.160 kyr. The grey solid line of $\eta_{\mathrm{AD,\,Ori}}$ implies the original ambipolar diffusivity unaffected by the AD dt floor. The cyan solid line of $\eta_{\mathrm{H,\,Ori}}$ implies the original Hall diffusivity unaffected by the Hall dt floor.

phase (∼20 kyr). The RSD accretes mass more rapidly from the collapsing envelope than it is able to transfer to the central stellar object,[3] and becomes self-gravitating. Ring-like structure (similar to Zhao et al. 2016) with large plasma-β (the ratio of thermal to magnetic pressure) of $\sim 10^3$–10^4 develops after ∼8 kyr of the first core formation, which would instead be an extended spiral structures in 3D simulations (Zhao et al. 2018a). Because of the low stellar mass, the gas rotation speed is mostly super-Keplerian, while remains gravitationally bound with $v_\phi \lesssim v_{\mathrm{Gp}} \equiv \sqrt{r\frac{\partial\Phi}{\partial r}}$ (Φ is the gravitational potential at radius r). Note that in this anti-aligned ($\boldsymbol{\Omega}\cdot\boldsymbol{B} < 0$) model, the disc rotation remains in the same direction as the initial core rotation, because the Hall effect in the inner envelope is to spin-up the rotation of the accreting flow.

4.2.2 *Aligned case* $\boldsymbol{\Omega}\cdot\boldsymbol{B} > 0$

We now turn to the aligned model 2.4opt3_AH$^+$O; the only difference in set-up from the 2.4opt3_AH$^-$O model above is the polarity of the magnetic field. As shown in Fig. 7, disc formation is initially suppressed during the first ∼4 kyr after the first core formation, followed by the formation of a counterrotating disc of ∼20 au radius. The process is largely similar to the early evolution of the aligned model demonstrated in Paper I (see their fig. 12) where only Hall and Ohmic are included. Basically, the azimuthal Hall drift enhances the bending of magnetic fields towards the direction of the initial rotation $+\phi$, which not only brakes the gas rotation along $+\phi$, but also reverses its direction to $-\phi$ within the inner ∼200 au. The azimuthal Hall drift velocity $v_{\mathrm{H},\phi}$ (indicated by $v_{\mathrm{BH},\phi} - v_\phi$) reaches values as large as ∼2–3 km s^{-1} in the inner tens of au, dominating the total azimuthal drift of magnetic fields $v_{\mathrm{d},\phi}$ ($\equiv v_{\mathrm{B,eff},\phi} - v_\phi$). Although the azimuthal ambipolar drift $v_{\mathrm{AD},\phi}$ is vanishing, it is still directed towards $-\phi$ (as $v_{\mathrm{B,eff},\phi} - v_{\mathrm{BH},\phi} < 0$), which is the opposite to the direction of the azimuthal Hall drift and hence tends to slightly relax the azimuthal bending of magnetic fields. In the radial direction, both ambipolar and Hall drift are directed along $+r$, working together to move the magnetic field radially outward relative to the infalling matter within $\lesssim 10^3$ au. Because of the enhanced azimuthal bending of magnetic fields by the azimuthal Hall drift in the aligned case, the induced radial Hall drift $v_{\mathrm{H,r}}$ is also somewhat larger than the radial ambipolar drift $v_{\mathrm{AD},r}$ (in contrast to the anti-aligned case where $v_{\mathrm{AD},r} > v_{\mathrm{H},r}$; Section 4.2.1).

---

[3] Initial RSDs formed in collapse simulations are generally massive, with moderate dependence on the sink treatment (Hennebelle et al. 2020). In this study, the disc to stellar mass ratio is further amplified by the 2D axisymmetric set-up that prevents mass accretion to the central stellar object via gravitational torques.

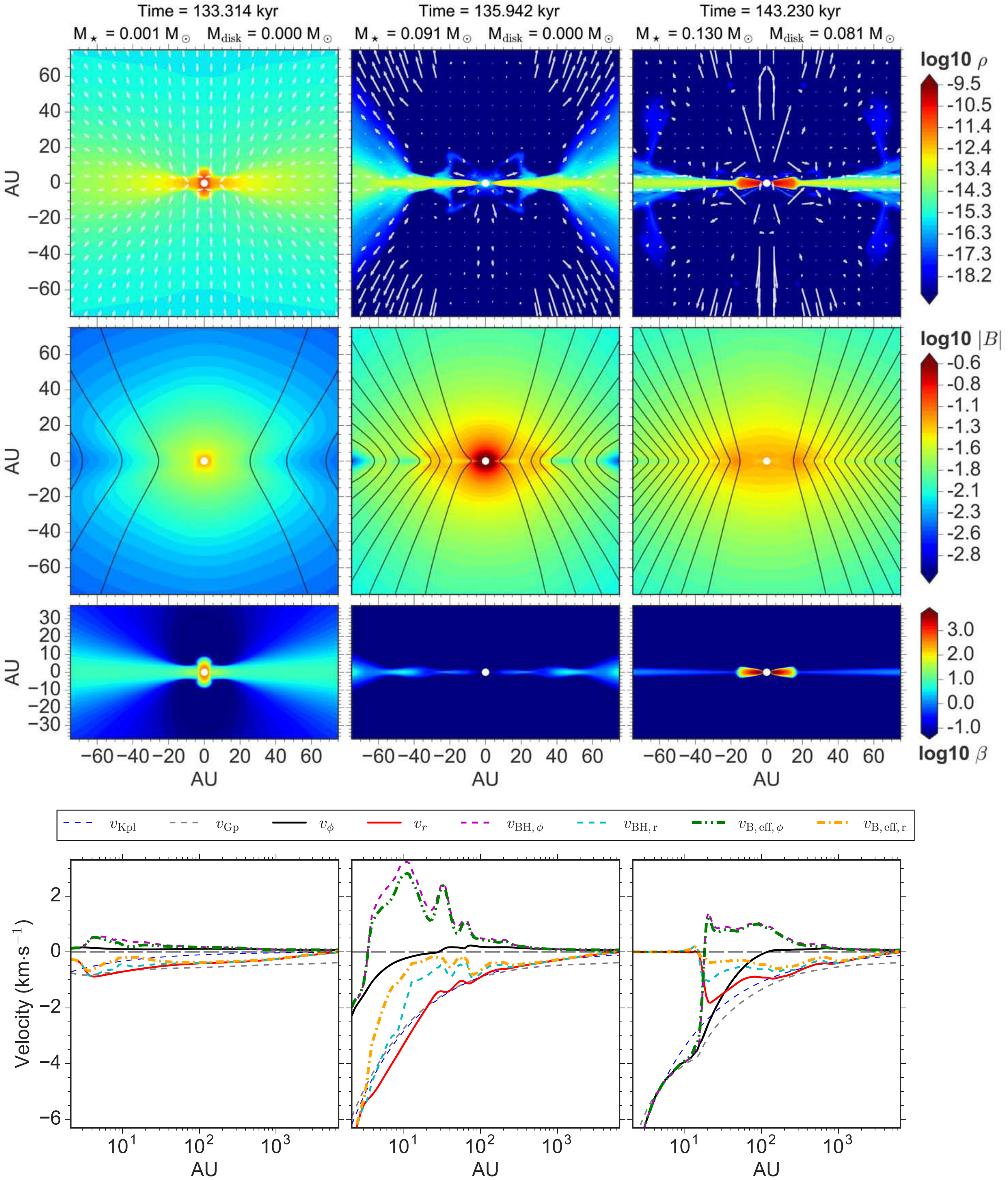

Figure 7. Evolution of disc in the aligned model 2.4opt3-H$^+$O. First row: logarithmic distribution of mass density along with velocity field vectors (white arrows). Second row: logarithmic distribution of total magnetic field strength $|B|$ along with magnetic field lines (black solid lines). Third row: logarithmic distribution of plasma-β. Fourth row: velocity profile along the equator. The abrupt change of infall speed v_r near the disc edge corresponds to the location of the centrifugal shock.

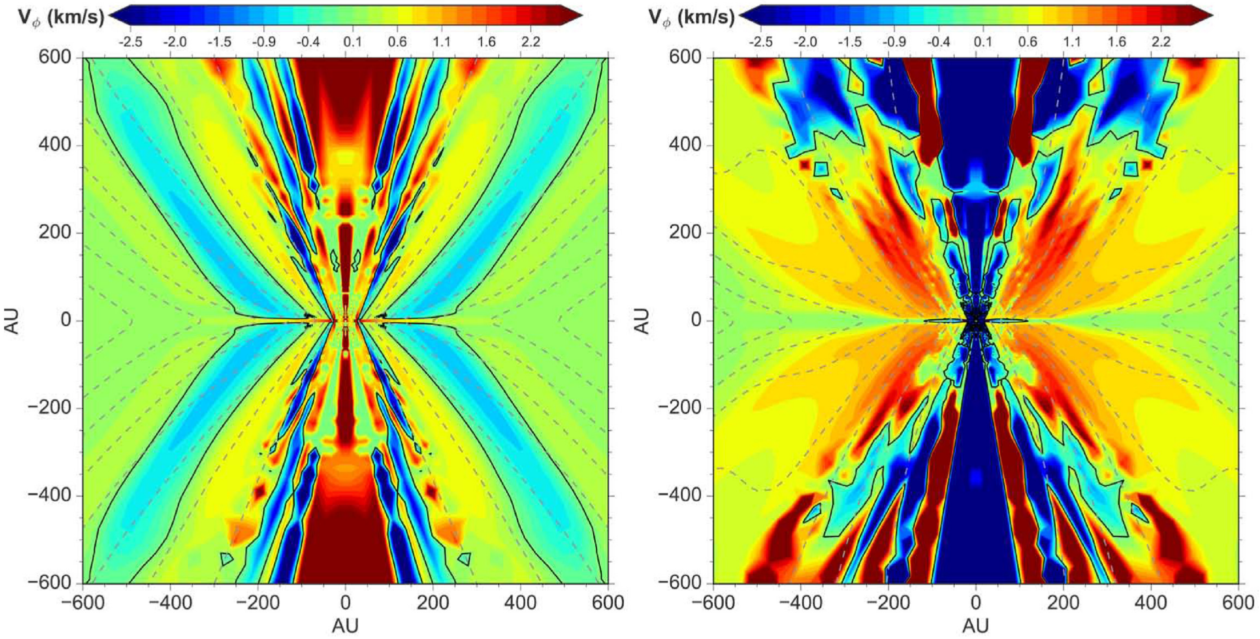

Figure 8. Distribution of azimuthal velocity v_ϕ at 600 au scale envelope for both the anti-aligned model 2.4opt3_AH$^-$O at $t = 142.280$ kyr (left-hand panel) and the aligned model 2.4opt3_AH$^+$O at $t = 143.230$ kyr (right-hand panel). Negative v_ϕ values represent rotation motion along $-\phi$ direction. The solid contour lines mark positions with $v_\phi = 0$, where the transition between positive and negative v_ϕ occurs. The grey dashed curves trace the magnetic field lines.

It is worth noting that the counterrotating RSD formed in the aligned case does not quickly become self-gravitating, and the disc mass remains below the stellar mass ($\sim$0.13 M$_\odot$) for as long as $\sim$10 kyr (after the disc formation). The low disc to stellar mass ratio is primarily because the central stellar object has already gathered sufficient mass during the initial disc suppression phase when the infalling gas is accreted easily into the inner boundary. However, as the counterrotating RSD develops, most of the infalling gas lands on the disc instead, and the stellar accretion slows down greatly (especially in the current 2D set-up). Because of the substantial stellar mass, the counterrotating RSD steadily grows in radius to $\sim$30 au without condensing into ring-like structures like in the anti-aligned case (Fig. 7). Again, the plasma-β along the disc mid-plane reaches $\sim 10^3$–10^4.

4.2.3 *Envelope rotation*

As demonstrated in Paper I (see also Krasnopolsky et al. 2011; Li et al. 2011; Tsukamoto et al. 2015b), Hall effect can induce counterrotating motions at the envelope scale by regulating the topology of the magnetic field; either a ‘butterfly-shaped’ thin shell is counterrotating (anti-aligned case) or the inner envelope enclosing the disc and outflow region is counterrotating (aligned case). Similar structures are present in both opt3 models here (2.4opt3_AH$^-$O and 2.4opt3_AH$^+$O), in which, despite the inclusion of AD as compared to Paper I without AD, Hall effect still dominates over AD in the inner envelope due to the choice of $a_{\min} = 0.03$ µm (rendering $\eta_{\rm H} > \eta_{\rm AD}$; Fig. 6). As shown in Fig. 8, in the anti-aligned case, v_ϕ becomes negative (along $-\phi$) within a thin shell in the range1000 au scale, while in the aligned case, v_ϕ is only negative along the inner $\lesssim$100 au equatorial region and along narrow stripes in the bipolar cavity. The extent of the counterrotating region in the anti-aligned case is similar to the Hall models in Paper I (see their fig. 10); for the aligned case, the counterrotating regions are somewhat smaller and less prominent comparing to the Hall models in Paper I in which the inner $\lesssim$200 au equatorial region and almost the entire bipolar cavity are counterrotating (see their fig. 14).

The presence of counterrotating regions in these Hall-dominated cases is a sign of angular momentum redistribution among different parts of the collapsing envelope by Hall effect. In the anti-aligned case, the negative angular momentum of the counterrotating shells spares the angular momentum budget needed for spinning up the gas rotation in the inner envelope and disc. In the aligned case, there is an excess of angular momentum at a few 10^2 au scale (reddish ‘butterfly-shaped’ lobes in the right-hand panel of Fig. 8), which compensates the negative angular momentum in the counterrotating inner equatorial and outflow region (see detailed discussions in Paper I). In either case, the deceleration or acceleration of gas rotation in the ‘butterfly-shaped’ envelope region is directed by the magnetic tension force in ϕ-direction, which is regulated by the azimuthal Hall drift $v_{{\rm H},\phi}$ that points to $+\phi$ in the anti-aligned case and $-\phi$ in the aligned case. These preferred directions of azimuthal Hall drift in the ‘butterfly-shaped’ regions are naturally derived from the convex-shaped (bending towards the equator) poloidal magnetic fields therein (Fig. 8; see also Paper I). Therefore, by choosing $a_{\min} = 0.03$ µm, Hall effect remains sufficient at the envelope scale to leave imprints on the angular momentum redistribution. However, it is no longer the case if a larger $a_{\min}$ is adopted, as we will discuss next in Section 4.3.

4.3 AD dominated collapse: unimodal disc rotation

As magnetic diffusivities are sensitive to the grain size distribution (Zhao et al. 2016; Dzyurkevich et al. 2017), we explore the trMRN models adopting $a_{\min} = 0.1$ µm, with which the ambipolar diffusivity $\eta_{\rm AD}$ reaches an optimal level throughout the collapsing envelope (Zhao et al. 2016), while the Hall diffusivity $\eta_{\rm H}$ drops by $\sim$1 order of magnitude below the optimal level of the opt3 models at densities

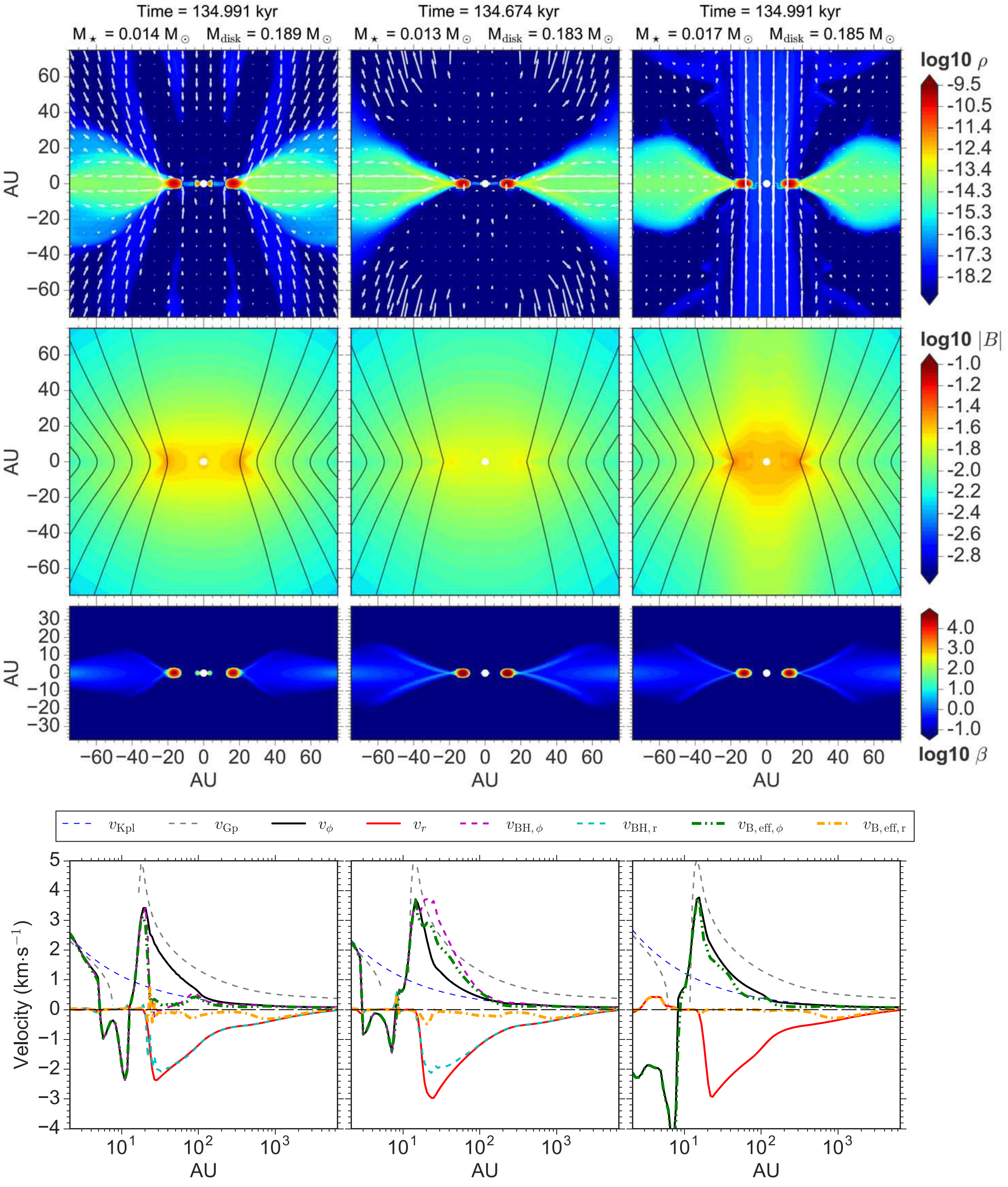

(a) **Anti-aligned: $\boldsymbol{\Omega}\cdot\boldsymbol{B}<0$** (b) **Aligned: $\boldsymbol{\Omega}\cdot\boldsymbol{B}>0$** (c) **AD model**

Figure 9. Disc formation in the trMRN models: anti-align case (left-hand panels), aligned case (middle panels), and case with only AD and Ohmic (right-hand panels). First row: logarithmic distribution of mass density along with velocity field vectors (white arrows). Second row: logarithmic distribution of total magnetic field strength $|B|$ along with magnetic field lines (black solid lines). Third row: logarithmic distribution of plasma-β. Fourth row: velocity profile along the equator. The abrupt change of infall speed v_r near the disc edge or ring structure corresponds to the location of the centrifugal shock.

$\lesssim 10^9$ cm^{-3} (see detailed discussions in Zhao et al. 2018b; Koga et al. 2019). Hence, in these trMRN models, AD dominates the diffusion of magnetic fields, while Hall effect plays a minor role and has little impact on the direction of gas rotation. As we show below, disc rotates along the same direction as the initial core, regardless of the polarity of the magnetic field.

Fig. 9 presents three trMRN models: the anti-aligned model 2.4trMRN_AH$^-$O, aligned model 2.4trMRN_AH$^+$O, and the comparison model 2.4trMRN_AO (without Hall effect), at a similar evolution stage when the total mass of the star and disc reaches $\sim$0.2 M$_\odot$. The disc morphology in the three models is nearly identical, showing as self-gravitating ring structures of $\sim$20 au radius

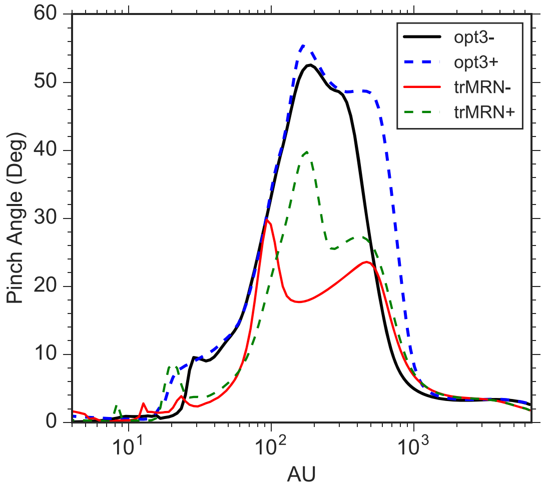

Figure 10. Radial profile of pinch angle of magnetic field lines. A larger pinch angle indicates a more severe radial pinch of the magnetic field lines. The black solid, blue dashed, red solid, and green dashed lines correspond to model 2.4opt3_AH$^-$O, 2.4opt3_AH$^+$O, 2.4trMRN_AH$^-$O, and 2.4trMRN_AH$^+$O, respectively.

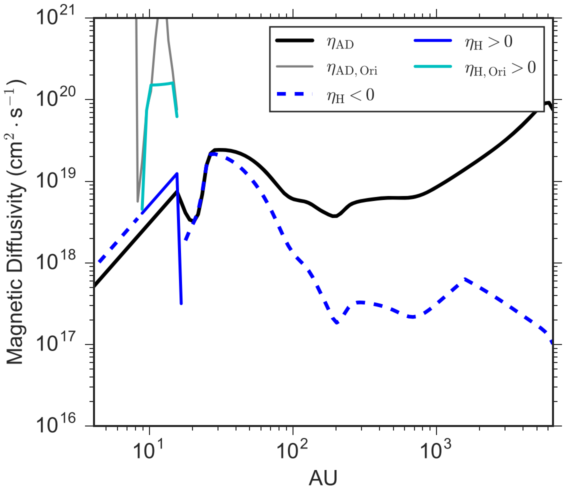

Figure 11. Same as Fig. 6, but for the equatorial magnetic diffusivities of the 2.4trMRN_AH$^+$O model at 134.674 kyr.

(that would be spirals or multiples in full 3D simulations; Zhao et al. 2018a). The gas rotation speed v_ϕ is positive (along $+\phi$) throughout the infalling envelope in all three models, and accordingly the ring structure is also rotating along $+\phi$. It is thus difficult to distinguish between the trMRN models with or without Hall effect, or to identify the polarity of the magnetic field, simply from the disc morphology and/or the direction of gas rotation. In fact, the three trMRN models also share a similar disc morphology and rotation direction with the anti-aligned model 2.4opt3_AH$^-$O in Section 4.2.1.

The formation of RSDs and rings in the trMRN models is mainly facilitated by the enhanced ambipolar diffusivity that causes large outward drift of magnetic fields at the envelope scale (see also Zhao et al. 2018a). As shown in Fig. 9, the effective velocity of the magnetic field lines in the radial direction $v_{\rm B,eff,\mathit{r}}$ nearly vanishes in the range ∼20–500 au along the pseudo-disc (equatorial plane) in all three models. While the radial drift of magnetic fields $v_{{\rm d},r}$ ($\equiv v_{\rm B,eff,\mathit{r}} - v_r$) in the Hall-free model (2.4trMRN_AO) is simply determined by the radial ambipolar drift that reaches ∼2–3 km s^{-1} in the inner tens of au, the dominant radial drift component in the trMRN models with Hall effect remains the ambipolar drift $v_{{\rm AD},r}$ (indicated by $v_{\rm B,eff,\mathit{r}} - v_{{\rm BH},r}$), which is around 2 km s^{-1} in the inner tens of au. In comparison, the radial Hall drift $v_{{\rm H},r}$ (indicated by $v_{{\rm BH},r} - v_r$) is mostly vanishing along the pseudo-disc and only reaches a few 0.1 km s^{-1} in the innermost tens of au. In any case, the net effect of ambipolar and Hall drift in the radial direction is to move the magnetic field outward relative to the infalling matter, for both the anti-aligned (.4trMRN_AH$^-$O) and aligned (.4trMRN_AH$^+$O) models. In particular, near ∼30 au where $v_{{\rm H},r}$ is non-vanishing, the radial ambipolar and Hall drift velocities are both positive (i.e. pointing towards $+r$), indicating a cooperative effort of AD and Hall effect radially within that equatorial section.

In the azimuthal direction, notable magnetic field drift only takes place in the inner 100 au, a smaller region than the opt3 models. Although the azimuthal Hall drift $v_{{\rm H},\phi}$ (indicated by $v_{{\rm BH},\phi} - v_\phi$) is the main contributor to the total azimuthal drift $v_{{\rm d},\phi}$ ($\equiv v_{\rm B,eff,\phi} - v_\phi$), the magnitude of $v_{{\rm H},\phi}$ is also smaller than that in the opt3 models. Recall that the azimuthal Hall drift velocity $v_{{\rm H},\phi}$ is proportional to the degree of radial pinching of magnetic fields (equation 7), which is now relaxed by the efficient AD in the trMRN models. In Fig. 10, we compare between the opt3 and trMRN models the pinch angle of magnetic field lines, which is defined as the angle between the vertical axis and the direction of the magnetic field just above and below the equatorial plane. The opt3 models show systematically larger pinch angles than the trMRN models by a factor of ∼2. The difference is the largest (∼20–30° difference) at the envelope scale (few 10^2 au) where the enhanced AD in the trMRN models already becomes efficient in radially decoupling the magnetic field ($v_{\rm B,eff,\mathit{r}} \rightarrow 0$) as compared to the much weaker AD in the opt3 models (Figs 4 and 7). At tens of au scale, the factor of ∼2 difference in the pinch angle is still visible (∼5° in the trMRN models versus ∼10° in the opt3 models), which can also be recognized by comparing the magnetic field geometries among Figs 4, 7, and 9. Thus, as AD becomes efficient, both the degree of radial pinching of magnetic fields and the induced azimuthal Hall drift $v_{{\rm H},\phi}$ are reduced. For the same reason, the magnetic field strength near the ring-like structure is also weaker in the trMRN models than in the opt3 models, by a factor of ∼10, which causes the plasma-β in the trMRN models to reach as high as ∼10^4–10^5.

It is worth noting that within the inner tens of au of the trMRN models with Hall effect, the azimuthal Hall and ambipolar drift operate counteractively, i.e. pointing towards opposite directions. For example, in the aligned model 2.4trMRN_AH$^+$O, the azimuthal Hall drift $v_{{\rm H},\phi}$ tends to increase the original bending of magnetic fields along $+\phi$ ($v_{{\rm BH},\phi} - v_\phi > 0$); however, the azimuthal ambipolar drift $v_{{\rm AD},\phi}$ sets to curb such a tendency by directing magnetic fields backward along -ϕ ($v_{\rm B,eff,\phi} - v_{{\rm BH},\phi} < 0$). In the anti-aligned model 2.4trMRN_AH$^-$O, similar counteractive interplay between the azimuthal Hall and ambipolar drift is marginally visible near ∼30 au, where magnetic fields become slightly bent towards $-\phi$ (so that the induced radial Hall drift is along $+r$). Note that, even with the enhanced ambipolar diffusivity, the 2.4trMRN_AO model (no Hall effect) shows little azimuthal ambipolar drift ($v_{{\rm AD},\phi} \lesssim 0.2$ km s^{-1}), as compared to the large radial ambipolar drift $v_{{\rm AD},r}$, which also reflects that the bending of magnetic fields is preferentially stronger in the radial direction than in the azimuthal direction.

In summary, AD is dominating the magnetic field evolution and promoting disc formation in the trMRN models, in contrast to the opt3 models where Hall effect plays the dominant role instead. Such a role switch between AD and Hall effect is directly caused by the change of the size distribution $a_{\rm min}$ from 0.03 to 0.1 μm. We show

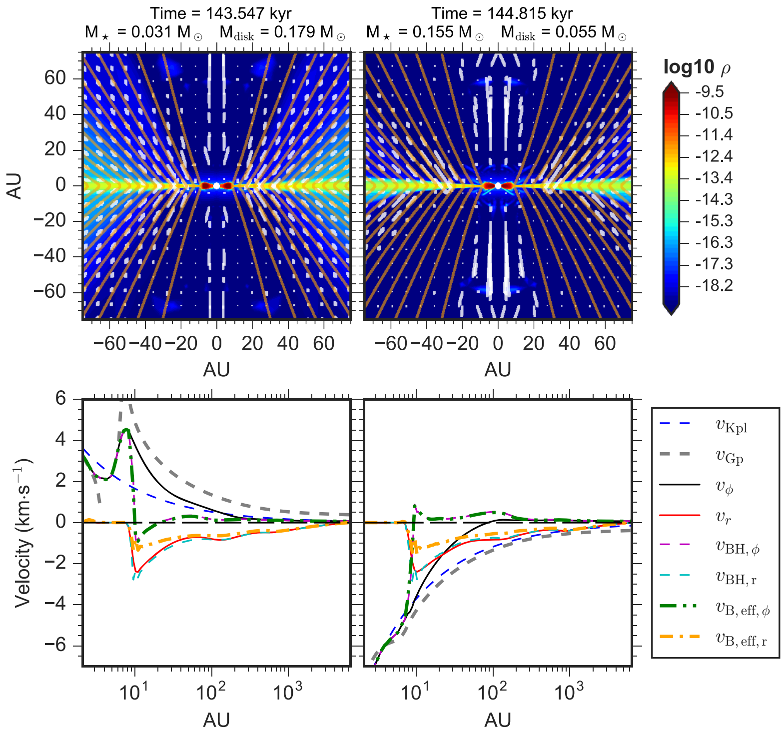

(a) Anti-aligned: $\boldsymbol{\Omega} \cdot \boldsymbol{B} < 0$ (b) Aligned: $\boldsymbol{\Omega} \cdot \boldsymbol{B} > 0$

Figure 12. Mass density distribution (top) and velocity profile along the equator (bottom) for model 2.4CR10opt3_AH$^-$O (left-hand panels) and model 2.4CR10opt3_AH$^+$O (right-hand panels). The white arrows and orange lines in the top panel are the velocity field vectors and magnetic field lines, respectively.

the magnetic diffusivities of the 2.4trMRN_AH$^+$O model in Fig. 11, in which the ambipolar diffusivity $\eta_{\rm AD}$ ($\gtrsim 10^{19}$ cm^2 s^{-1}), is ∼1–2 orders of magnitude larger than the Hall diffusivity $\eta_{\rm H}$ (∼few 10^{17} to few 10^{18} cm^2 s^{-1}) throughout the envelope (outside the disc); $\eta_{\rm H}$ only starts to catch up with $\eta_{\rm AD}$ within the inner tens of au. Recall that in the opt3 models (Fig. 6), $\eta_{\rm H}$ is instead dominating over $\eta_{\rm AD}$ in the inner envelope. Moreover, $\eta_{\rm H}$ of the trMRN models only becomes comparable to that of the opt3 models within the inner 100 au scale, where the Hall drift velocities become notable in Fig. 9 of the trMRN models.

Finally, as a result of the strong AD and weak Hall effect in the trMRN models, there is no clear signature of counterrotating motion in the collapsing envelope, in contrast to the well-established counterrotating regions in both the aligned and anti-aligned opt3 models (see Section 4.2.3).

4.4 High cosmic-ray ionization rate: reduced magnetic field drift and small disc

We now explore the case of higher CR ionization rate, i.e. $\zeta_0^{\rm H_2} = 10^{-16}$ s^{-1}, with which the magnetic diffusivities are overall lower by a factor of ∼2–3 than with the canonical 10^{-17} s^{-1} ($\propto \sqrt{\zeta_0^{\rm H_2}}$; Umebayashi & Nakano 1990) throughout the collapsing envelope. In either the aligned or anti-aligned case (Fig. 12), a small compact RSD is formed, with radius remained around ∼10 au till the end of the simulation (∼20 kyr after the first core formation). Despite the reduced diffusivity, the azimuthal Hall drift velocity can still efficiently regulate the magnetic field in the azimuthal direction, causing the gas rotation in the inner envelope to either spin-up or down depending on the polarity of the magnetic field. Similar to the opt3 models with a canonical $\zeta_0^{\rm H_2}$ (Section 4.2; canonical-opt3 models for short), the resulting disc can either rotate along $+\phi$ in the anti-aligned case (2.4CR10opt3_AH$^-$O) or along $-\phi$ in the aligned case (2.4CR10opt3_AH$^-$O).

As shown in Fig. 12, the total azimuthal drift is primarily determined by the azimuthal Hall drift, while the azimuthal ambipolar drift is vanishing. The magnitude of the azimuthal Hall drift velocity $v_{{\rm H},\phi}$ is somewhat smaller (by a factor of ∼2) in comparison to the opt3 models with a canonical $\zeta_0^{\rm H_2}$ (Figs 4 and 7). In the radial direction, the total radial drift is dominated by the radial ambipolar drift, whereas the radial Hall drift is negligible. The radial ambipolar drift velocity $v_{{\rm AD},r}$ is also somewhat smaller than that of the canonical-opt3 models; however, the radial ion-neutral decoupling already starts in the low-density envelope from ∼800 au – similar scale as in the canonical-opt3 models. Although the radial Hall drift is barely non-vanishing within the inner ≲100 au scale, its direction is consistent with that demonstrated in the canonical-opt3 models in Section 4.2, i.e. $v_{{\rm H},r}$ in the inner envelope points radially inward in the anti-aligned case and radially outward in the aligned case. Nevertheless, the total radial drift $v_{{\rm d},r}$ dominated by AD is still moving the magnetic field radially outward relative to the infalling matter, but in a reduced speed compared with the opt3 models with a canonical $\zeta_0^{\rm H_2}$.

In terms of disc formation, these opt3 models with a higher CR ionization rate ($\zeta_0^{\rm H_2} = 10^{-16}$ s^{-1}) lie in between the MRN models (Section 4.1) and the opt3 models (Section 4.2) with the canonical CR ionization rate. This is caused by the variations in microphysics. In comparison to the MRN models (Fig. 3), these opt3 models with a high CR ionization rate (Fig. 13) still have a twice larger $\eta_{\rm H}$ within the inner ≲100 au (a few 10^{18} cm^2 s^{-1}), and a ∼10 times larger $\eta_{\rm AD}$ in the envelope scale beyond ≳100 au. The radial ambipolar

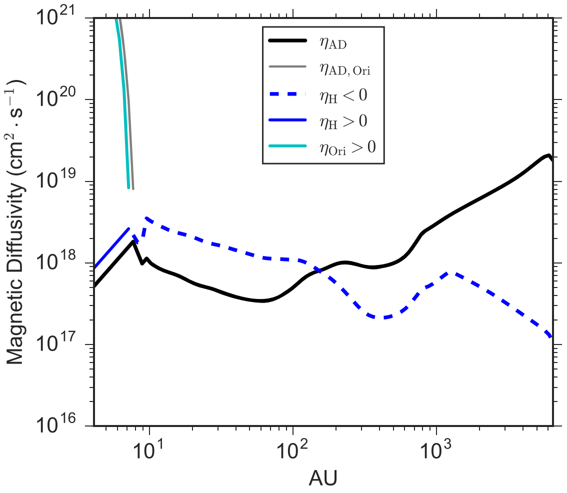

Figure 13. Same as Fig. 6, but for equatorial magnetic diffusivities of the 2.4CR10opt3_AH$^+$O model at 144.815 kyr.

drift throughout the infalling envelope along with the azimuthal Hall drift in the innermost envelope together enable the formation of the small compact RSDs in these high CR models. We have explored models with even higher $\zeta_0^{\rm H_2}$, and find that when $\zeta_0^{\rm H_2}$ is above 2–3 × 10^{-16} s^{-1}, $\eta_{\rm AD}$ and $\eta_{\rm H}$ becomes comparable to that of the MRN models, so that disc formation is strongly suppressed in such axisymmetric set-ups. Note that the conditions of $\zeta_0^{\rm H_2}$ for disc formation is slightly more stringent if Hall effect is excluded, with a threshold of a few 10^{-17} s^{-1} derived in Zhao et al. (2016, see also Kuffmeier, Zhao & Caselli 2020).

4.5 Impact of initial conditions and grain size limit

Previous sections focus on the representative models in the strong field case ($\lambda \sim 2.4$); in this section, we summarize results of the other models in Tables 1–3, and demonstrate how AD and Hall effect affect disc formation and morphology in different parameter space.

As shown in Paper I (see also Wurster & Bate 2019), decreasing the initial magnetic field strength weakens Hall effect in general. For the opt3 models ($a_{\rm min} = 0.03$ µm) in which Hall drift is the most efficient, disc morphology in the anti-aligned case is relatively unaffected by the change of magnetic field strength; the anti-aligned opt3 models mostly form 20–30 au ring-like structures (spirals/multiples in 3D that becomes more gravitationally unstable as the core magnetization weakens; Zhao et al. 2018a). However, for the aligned opt3 models, weakening the initial magnetic field strength indeed hinders the formation of the counterrotating disc.[4] For example, the radius of the counterrotating disc is only ~20 au in the 4.8opt3_AH$^+$O model, compared with the ~30 au counterrotating disc in the 2.4opt3_AH$^+$O model. In the very weak field ($\lambda \sim 9.6$) model 9.6opt3_AH$^+$O, no clear counterrotating motion develops in the inner envelope and only a ring-like structure forms, which rotates along the direction of initial core rotation ($+\phi$); it is thus difficult to determine the magnetic field polarity from the disc morphology in the very weak field case. Basically, in weaker field models, the azimuthal Hall drift becomes less efficient, and the tension force directed towards $-\phi$ in the aligned cases also becomes weaker, or even fails to brake the original gas rotation along $+\phi$ in the very weak field case ($\lambda \sim 9.6$). The main role of Hall effect in the 9.6opt3_AH$^+$O model is instead to drift the magnetic field radially outward, similar to the weak field model (without AD) presented in Paper I.

For the trMRN models in which AD is the most efficient, weakening the initial magnetic field strength results in somewhat larger RSDs or ring-like structures, consistent with the parameter study of Zhao et al. (2016, 2018a) without Hall effect. Again, the disc morphology across the trMRN models is insensitive to Hall effect and hence the magnetic field polarity, as the poloidal magnetic fields are efficiently drifted radially outward by the enhanced AD (see Section 4.3).

For the MRN models and the models with very high-CR ionization rate ($\zeta_0^{\rm H_2} = 5 \times 10^{-16}$ s^{-1}) where disc formation is suppressed, weakening the initial magnetic field strength increases the radius of the initial disc structure formed shortly after the first core. However, with the low level of magnetic diffusivities, the initial disc structures in the MRN models and the high CR models typically shrink in radius over time, as collapse drags more magnetic flux into the central disc forming region (see also Zhao et al. 2016, 2018a; Lam et al. 2019). It is only in models with $\zeta_0^{\rm H_2} = 10^{-16}$ s^{-1} that a small compact disc of ~10 radius survives, for both strong and weak magnetic field.

We also explore the collapse of initially non-rotating cores for the grain size distributions of opt3 and trMRN. Sizable RSDs of ~30 au radius is able to form in the non-rotating opt3 models (both strong and weak field) due to the large Hall diffusivity. The rotational motion in the inner envelope and hence the disc is essentially generated by Hall effect, which causes the radially pinched magnetic field lines to become bended azimuthally along the direction of the azimuthal Hall drift ($+\phi$). The resulting tension force then spins up the gas rotation in the inner envelope towards the opposite direction ($-\phi$) of the azimuthal Hall drift. In contrast, in the non-rotating trMRN models (either strong or weak field) where AD dominates the collapse, the weak Hall effect only slightly spins up the gas rotation along $-\phi$, but not enough to form any rotationally supported structure.

Finally, we find that the lower limit of $a_{\rm min}$ above which disc formation by non-ideal MHD effects becomes possible is around $\lesssim$10 nm, similar to that discussed in Paper I where AD is ignored. Note that such a limit is less stringent than that derived in the Hall-free study of Zhao et al. (2016), where the lower limit of $a_{\rm min}$ was a few times larger. For the min1 models in Tables 1–2 with $a_{\rm min}$ set to 10 nm, the ambipolar diffusivity is not much different from the MRN models, and efficient radial drift by AD only occurs along the pseudo-disc within the inner $\lesssim$100 au scale. However, the Hall diffusivity is already enhanced by ~1 order of magnitude relative to the standard MRN size distributions at densities above $\gtrsim 10^9$ cm^{-3} (corresponding to the inner $\lesssim$200 au pseudo-disc region; see also Dzyurkevich et al. 2017; Zhao et al. 2018b). Therefore, both ambipolar diffusion and Hall effect are efficient within $\lesssim$100 au scale, which enables formation of RSDs in the min1 models. Nonetheless, the requirements on microphysics for disc formation, particularly $a_{\rm min}$ and $\zeta_0^{\rm H_2}$ (Section 4.4), are somewhat relaxed by the inclusion of Hall effect, in comparison to studies focused only on AD.

4.6 Outflow morphology

Because microphysics modulates the synergy between AD and Hall effect, which profoundly affects the magnetic field strength and topology, the bipolar outflows hence manifest diverse morphologies

---

[4] For the aligned model 4.8opt3_A$^+$H, a normally rotating disc of ~15 au forms initially but shrinks over time towards the central stellar object. It is possible that the star itself (and materials close to the star) can spin in the opposite direction of the counterrotating disc, but the same direction as the bulk envelope material.

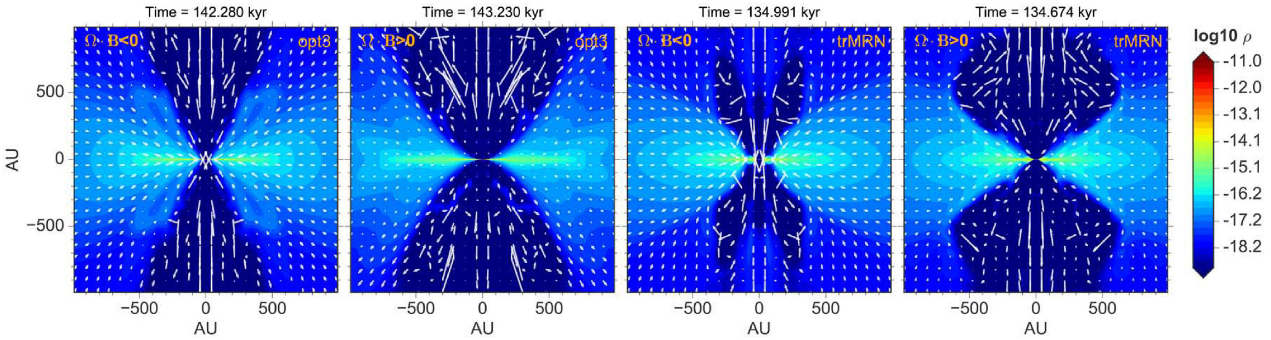

Figure 14. Bipolar outflows at 1000 au scale for model 2.4opt3_AH$^-$O at t = 142.280 kyr (first panel from left), 2.4opt3_AH$^+$O at t = 143.230 kyr (second panel), 2.4trMRN_AH$^-$O at t = 134.991 kry (third panel), and 2.4trMRN_AH$^+$O at t = 134.674 kyr (fourth panel), respectively. Velocity field vectors are shown in white arrows. The total mass of star and disc is similar among the four frames, implying a similar evolution stage.

and properties for different grain size distributions and magnetic field polarities.

As shown in Fig. 14, the aligned cases ($\boldsymbol{\Omega} \cdot \boldsymbol{B} > 0$) preferentially show wider outflow cavities than the anti-aligned cases ($\boldsymbol{\Omega} \cdot \boldsymbol{B} < 0$), with either opt3 or trMRN grains. This is an outcome of the regulation of B_ϕ by the azimuthal Hall drift, which tends to enhance B_ϕ towards the direction of the initial rotation $+\phi$ in the aligned cases, but to weaken B_ϕ with $v_{\mathrm{H},\phi}$ pointing towards $-\phi$ in the anti-aligned cases (see Figs 4, 7, and 9). Such an enhancement and weakening of the toroidal magnetic field by Hall effect then determines the strength and open-angle of the centrifugal driven outflows (Blandford & Payne 1982; Pelletier & Pudritz 1992; Tomisaka 2002; Seifried et al. 2012). Indeed, the outflow velocity at few 100 au scale above the disc plane is only ∼1–2 km s^{-1} in the anti-aligned model 2.4opt3_AH$^-$O, which is a factor of 2–3 slower than in the aligned model 2.4opt3_AH$^+$O (∼4–6 km s^{-1} at the same scale). Furthermore, because the disc in the aligned model is counterrotating, the outflow region near the bipolar axis is also counterrotating with respect to the bulk envelope (see Fig. 8); this can be an observable feature (Takakuwa et al. 2018) for identifying the polarity of the magnetic field in the Hall-dominated collapse.

Furthermore, switching the grain size distribution from opt3 to trMRN generally reduces the outflow velocity by a factor of ∼2 for both polarities of the magnetic field. The strong AD operating in the trMRN models decreases the amount of magnetic flux dragged into the inner envelope (hence reducing the magnetic field strength; Zhao et al. 2018a), and also lowers the degree of radial pinching of poloidal magnetic fields (see Fig. 10); both factors tend to suppress the launching of centrifugal driven outflows (see also discussions in Marchand et al. 2020; Tsukamoto et al. 2020). In Fig. 14, the outflow cavities in the trMRN models extend to a lower height vertically than in the opt3 models. Note that the trMRN models mostly form ring-like structures (spirals/multiples in 3D), which may also disfavour strong outflows in comparison to a compact disc structure.

5 DISCUSSION

5.1 Comparison with Hall-only models

We have shown in Paper I that, in the absence of AD, Hall effect can only produce small ≲10–20 au discs, regardless of the magnetic field polarity. The small disc radii are caused by the development of the so-called 'RSHCS' (rotationally supported Hall current sheet) surrounding the inner disc during the main accretion phase. Within the RSHCS, highly pinched poloidal magnetic fields are moving radially inward relative to matter, flattening the RSHCS region into a thin sheet-like structure.

In this study, the presence of AD largely suppresses the development of RSHCS,[5] as the radial ambipolar drift efficiently slows down the inward drift of magnetic fields by Hall effect at tens of au scale, so that the total radial drift is mostly pointing outward (Figs 4 and 7). The RSDs formed in this study are generally larger in radius than in Paper I, and would likely develop extended spiral structures or become multiple systems in full 3D set-ups (Zhao et al. 2018a; Wurster & Bate 2019). Therefore, persistent outward diffusion of magnetic field in the radial direction remains crucial for disc formation and growth.

Another point worth noting is that the processes of protostellar collapse and disc formation between the opt3 and trMRN models in Paper I (without AD) behave similarly, with the opt3 models forming slightly larger disc sizes than the trMRN models (see tables 1 and 2 in Paper I) due to the differences in η_{H}. However, as we have shown in this study (with AD), changing the minimum grain size from 0.03 µm (opt3) to 0.1 µm (trMRN) causes the collapse to switch from Hall-dominated to AD-dominated; the morphologies and kinematics of the envelope and disc show clear differences between the two types of collapse.

Similar to Paper I, we illustrate the general configuration of the magnetic field under the complex regulation of ambipolar and Hall drift, for the Hall-dominated collapse (the illustration of an AD dominated collapse is much simpler). In Figs 15 and 16, the directions of ambipolar and Hall drift in different sections of the inner envelope and disc follow the same basic principles derived in Section 2.1 (see Fig. 1). The combined effort of AD and Hall effect is to drift the magnetic field against the primary direction of field bending by the dominant dynamical process, i.e. gravitational collapse in the envelope or Keplerian rotation in the disc. Note that due to the severe azimuthal bending of magnetic fields ($\frac{\partial B_\phi}{\partial z}$) inside the disc, the radial Hall drift usually dominates the radial ambipolar drift therein.

It is also clear from such illustrations that the disc formed from a Hall-dominated collapse can only have one particular magnetic field polarity ($\boldsymbol{\Omega} \cdot \boldsymbol{B} < 0$; see also discussions in Paper I). Accordingly, the magnetic field along the disc mid-plane tends to drift radially outward by Hall effect (Bai & Stone 2017). However, this would not be the case for an AD-dominated collapse or a weakly magnetized core,

---

[5] Transient RSHCS-like features do occasionally appear in this study, but are only limited to narrow regions (width ≲1 au) near the disc edge, where the total radial drift points briefly inward. Such transient features is unlikely to affect the disc formation, yet they may not be numerically resolved with the current set-up.

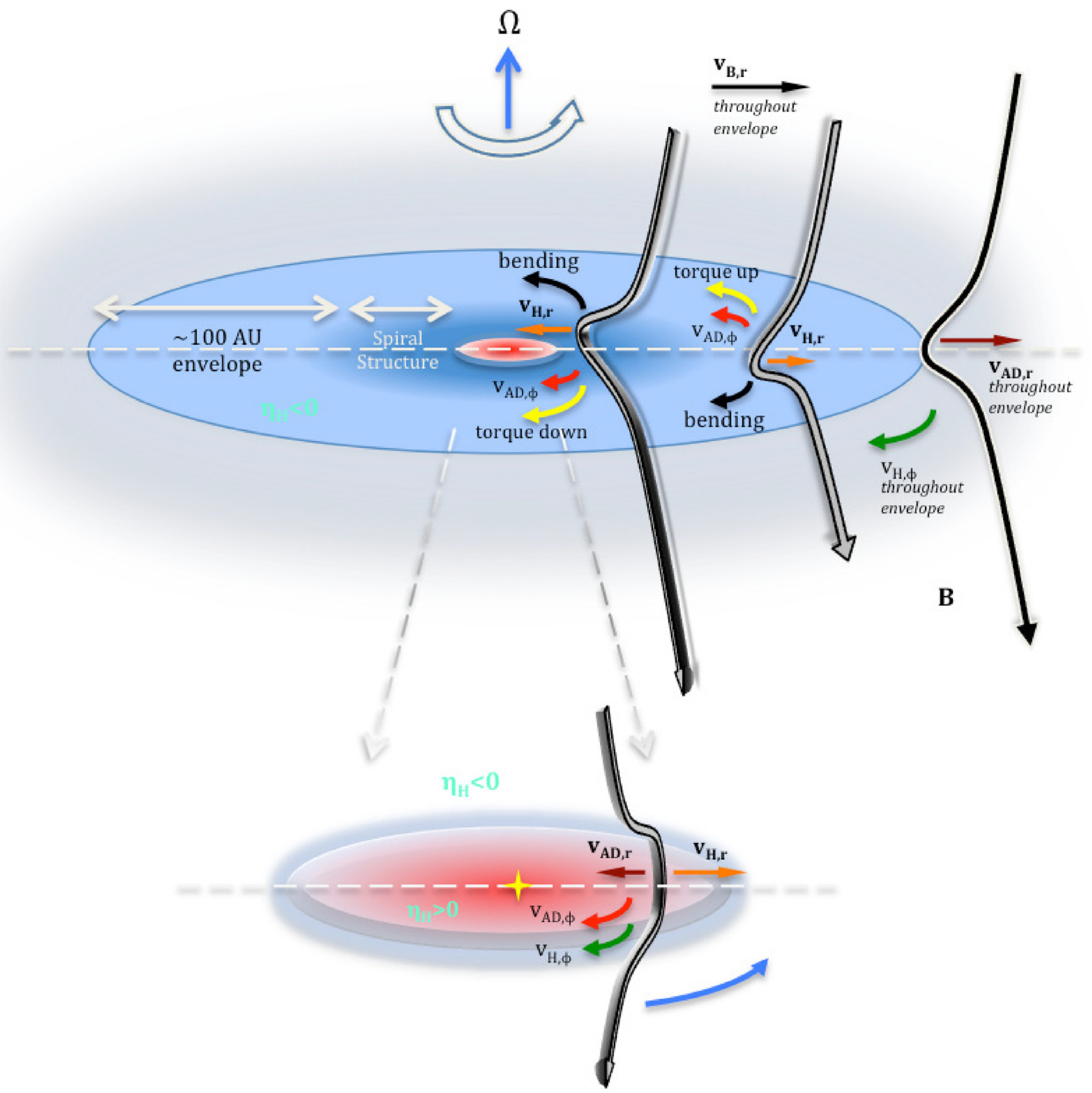

Figure 15. Sketch of magnetic field morphologies in the inner envelope (top) and in the disc (bottom) for the anti-aligned case ($\boldsymbol{\Omega} \cdot \boldsymbol{B} < 0$) in the Hall-dominated collapse. Note that $\eta_{\rm H}$ changes sign across the disc boundary, and that the actual value of $v_{{\rm AD},\phi}$ in the top panel is vanishing (see Fig. 4).

since the eventual disc rotation is little affected by Hall effect during the collapse, and both $\boldsymbol{\Omega} \cdot \boldsymbol{B} < 0$ and $\boldsymbol{\Omega} \cdot \boldsymbol{B} > 0$ become possible. Therefore, the magnetic field polarity as well as the direction of field diffusion in protoplanetary discs are closely related to how discs are formed from the protostellar collapse and what microphysics are considered in the protostellar envelope. Finally, across the disc boundary (either radially or vertically), $\eta_{\rm H}$ changes sign as Hall drift switches from being dominated by the drift of positively charged species (e.g. ions) relative to negatively charged species (e.g. negatively charged grains) to being dominated by the usual electron-ion drift (Paper I; see also Xu & Bai 2016; Lesur 2020), which could potentially affect the development of the so-called 'Hall-shear' instability (Kunz 2008) across the disc surface (Bai & Stone 2017).

5.2 Disc to stellar mass ratio

Across the Hall-dominated models with $a_{\rm min} = 0.03$ µm, not only the direction of disc rotation is bimodal, the disc to stellar mass ratio also bifurcates: the ratio is much larger than unity in the anti-aligned case ($\boldsymbol{\Omega} \cdot \boldsymbol{B} < 0$), and is lower or close to unity in the aligned case ($\boldsymbol{\Omega} \cdot \boldsymbol{B} > 0$). The difference is mainly caused by the amount of mass accumulated in the central stellar object at early times shortly after the first core formation. Although the 2D axisymmetric set-up generally hinders the stellar mass accretion, a considerable amount of mass (0.1–0.2 $\mathrm{M}_{\odot}$) is able to accrete on to the central stellar object in the aligned opt3 models (Section 4.2.2) during the initial disc suppression phase. In contrast, the stellar mass remains relatively small in the anti-aligned opt3 models and the RSDs are mostly self-gravitating.

However, we expect such a bifurcation of disc to stellar mass ratio to be somewhat alleviated in full 3D simulations, as asymmetric structures such as spirals promote the mass accretion into the central stellar vicinity for both the anti-aligned and aligned cases. In fact, how mass is funnelled from discs to protostars remains a debated topic (Takasao et al. 2018). With a limited resolution in protostellar collapse simulations, artificial sinks are usually introduced to model the central stellar object. In this study,

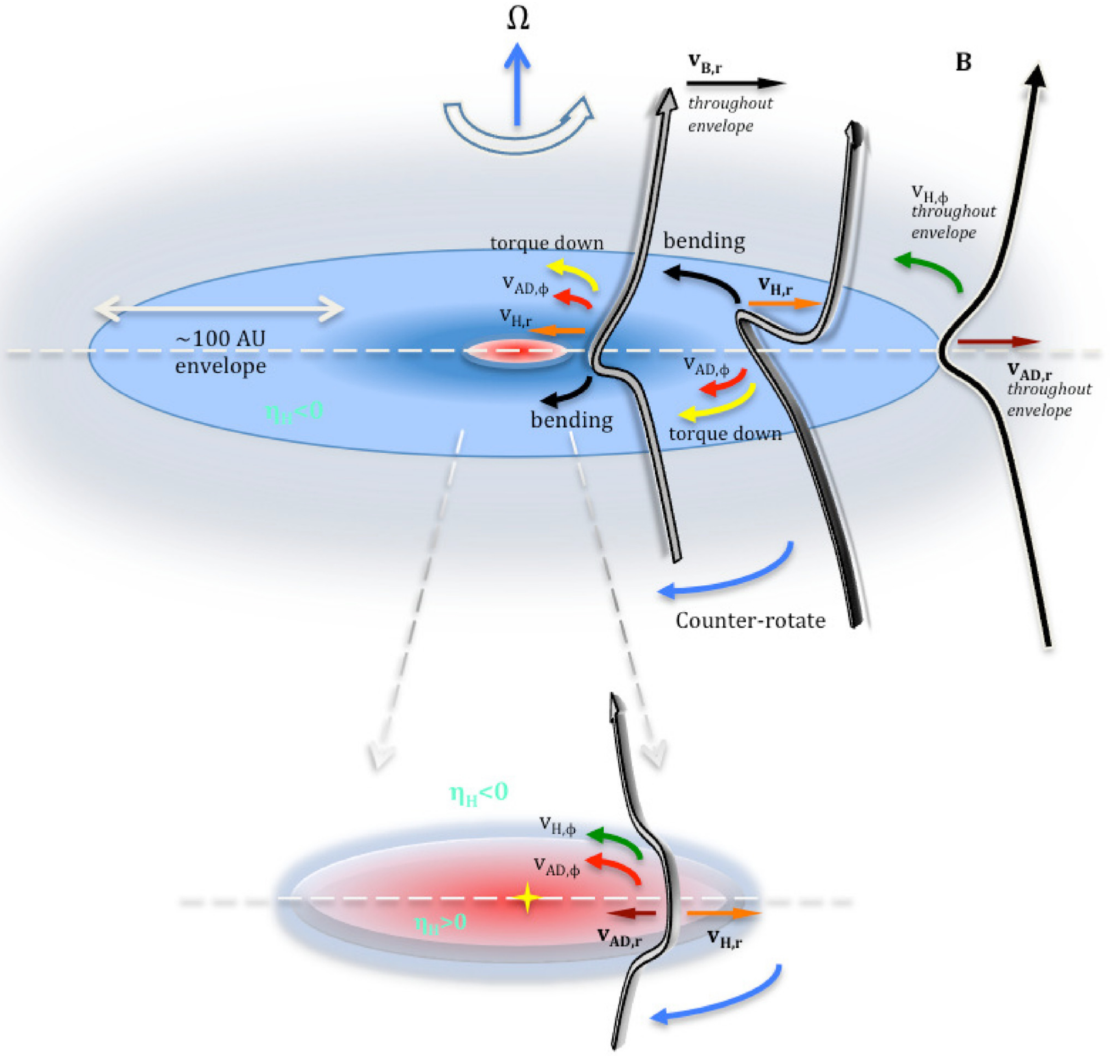

Figure 16. Same as Fig. 15, but for the aligned case ($\boldsymbol{\Omega} \cdot \boldsymbol{B} > 0$) in the Hall-dominated collapse. Note that in the top panel, the bending of the leftmost field line towards $-\phi$ tends to torque down the counterrotation.

we consider mass falling into the inner boundary ($r_{\rm in} = 2$ au) as being accreted by the central stellar object. It is obvious that the larger the inner boundary, the easier it is for the central stellar object to grow in mass (e.g. Krasnopolsky et al. 2011; Li et al. 2011 adopted $r_{\rm in} \sim 6.67$ au). As a result, the disc to stellar mass ratio is also dependent on the size of the inner boundary. Similar phenomenon is often discussed in studies using sink particles to model the central stellar object (Machida, Inutsuka & Matsumoto 2014; Hennebelle et al. 2020), in which typical parameters of the sink treatment including accretion radius and threshold density can have a substantial impact on both disc formation (Machida et al. 2014) and disc to stellar mass ratio (Hennebelle et al. 2020). Essentially, decreasing the threshold density and/or increasing the accretion radius facilitate the mass growth of the central stellar object, but suppress the disc to assemble mass, especially in the ideal MHD limit.

Nevertheless, it would be important to explore in 3D the relation between the disc to stellar mass ratio and the magnetic field polarity in a Hall-dominated collapse, as well as how much the inner boundary or sink treatment can affect such a relation. Future studies along this line could offer critical guidance for observations to constrain the masses of Class 0/I protostellar discs (Manara, Morbidelli & Guillot 2018; Ballering & Eisner 2019).

5.3 Comparison with other studies

The importance of microphysics in disc formation, including grain size distribution and CR ionization rate, has only been explored by different groups since recently (Padovani et al. 2014; Zhao et al. 2016; Marchand et al. 2020; Tsukamoto et al. 2020), as earlier work suggested that an enhanced resistivity is necessary to enable the formation of sizable RSDs (Shu et al. 2006; Krasnopolsky et al. 2010). However, difference in the chemistry networks and cloud initial conditions can often lead to different conclusions.

Tsukamoto et al. (2020) showed that tens of au RSDs can still form with the standard MRN size distribution, which is mainly due to their choice of a centrally concentrated density profile (Bonnor–Ebert sphere) combined with a uniform magnetic field. Such an initial set-up is shown by previous studies (Machida et al. 2014; Lam et al. 2019) to facilitate disc formation even with the fiducial level of ambipolar diffusivity from Shu (1991), whose magnitude is comparable to that derived using the standard MRN size distribution at the envelope density (10^6–10^9 cm^{-3}; Zhao et al. 2018b). As pointed out by Machida et al. (2014), the mass-to-flux ratio near the cloud centre is higher in the Bonner–Ebert sphere set-up than in the uniform sphere set-up, by a factor of ∼2–3, even if the global mass-to-flux remains the same for the two set-ups. Ideally, a more self-consistent distribution of the magnetic field strength and geometry (e.g. 'hourglass-shaped') should be initialized for clouds with a centrally concentrated density profile; otherwise, initializing a uniform magnetic field would have assumed that mass has concentrated in the cloud centre without dragging in the magnetic field.

Furthermore, the ambipolar diffusivities obtained from the ionization chemistry of Tsukamoto et al. (2020) is mostly lower than Shu's fiducial $\eta_{\rm AD}$ level by 1–2 orders of magnitude, the opposite to the results of other studies (e.g. Dzyurkevich et al. 2017; Zhao et al. 2018b). In fact, disc formation has been shown to be strongly suppressed with an $\eta_{\rm AD}$ profile below the Shu's fiducial level (Mellon & Li 2009; Li et al. 2011; Lam et al. 2019). Hence, it is important to ensure that the ionization chemistry converges among different groups. Note that it is also unclear in Tsukamoto et al. (2020) how the magnetic flux is treated when matter is accreted on to the sink particle, the lack of 'DEMS' (Decoupling-Enabled Magnetic Structures; Zhao et al. 2011; Krasnopolsky et al. 2012; Hennebelle et al. 2020; Machida & Basu 2020) across their models may suggest a deletion of the magnetic flux associated with the accreted matter (similar to Wurster, Price & Bate 2017), which further helps RSDs to form and survive even with a relatively low magnetic diffusivity.

The series of non-ideal MHD core collapse simulations using RAMSES (Masson et al. 2016; Hennebelle et al. 2020; Marchand et al. 2020) mostly adopt the ionization chemistry from Marchand et al. (2016), in which a modified MRN size distribution ($a_{\rm min} = 0.0181$ μm and $a_{\rm max} = 0.9049$ μm) is used to compute the magnetic diffusivities. As pointed out by Zhao et al. (2016), such a modified MRN distribution already overperforms (in terms of $\eta_{\rm AD}$) the standard MRN distribution as well as the Shu's fiducial level by up to a factor of 10 in the inner envelope and disc scales. Tens of au RSDs are expected to form under such an enhanced diffusivity (Fig. 17). The analytical formula derived in Hennebelle et al. (2016) adopts a relatively high $\eta_{\rm AD}$ of 7.16×10^{18} cm^2 s^{-1}. In addition, Hennebelle et al. (2020) set an initial misalignment angle of 30° between the magnetic field and rotation, which also makes disc formation easier than the axisymmetric set-ups (Joos et al. 2012; Li et al. 2013).

In comparison to our previous work (Zhao et al. 2016, 2018a), the inclusion of Hall effect relaxes the requirements on microphysics for disc formation (Sections 4.4 and 4.5). In particular, (1) the lower limit of $a_{\rm min}$ reduces from a few times 10 nm to just $\lesssim$10 nm, i.e. truncating off the tiny grains (e.g. PAHs) at the lower end of the MRN size distribution is already enough for non-ideal MHD effects to promote disc formation; (2) the upper limit of $\zeta_0^{\rm H_2}$ increases to 2–3 $\times$ 10^{-16} s^{-1}, a factor of 10 larger than the limit derived in our Hall-free study (Zhao et al. 2016), but with a $\zeta_0^{\rm H_2}$ close to the upper limit, only compact discs of $\lesssim$10 au radius could form. Given the observational evidence of depletion of $\lesssim$10 nm VSGs in dense molecular cores (Tibbs et al. 2016), and the typical range of CR ionization rate in dense cores (few 10^{-18} s^{-1} to few 10^{-16} s^{-1}; Caselli et al. 1998; Padovani, Galli & Glassgold 2009), the new requirements on microphysics basically imply a universality of RSDs around low-mass protostars. The spread in disc radius and morphology of nearby protostellar sources is likely a result of different cloud initial conditions, especially the environmental factors such as CR ionization rate (Kuffmeier et al. 2020). For example, sources with small discs (e.g. B335) may indicate a higher CR ionization rate at the cloud scale (Yen et al. 2019, 2020), while regions with $\zeta_0^{\rm H_2}$ close to the canonical value of 10^{-17} s^{-1} allow both small and large discs or multiple systems to form (Tobin et al. 2016; Segura-Cox et al. 2018), depending on other initial parameters (Zhao et al. 2018a) such as magnetic field strength, rotation speed, density perturbation, as well as the degree of misalignment between the magnetic field and rotation.

Finally, the recent discovery of a $\sim$$10^4$ au streamer in the protostellar envelope of IRAS 03292+3039 (Pineda et al. 2020) opens a new window for studying protostellar collapse and disc formation. Since individual star-forming cores are often not isolated from the large-scale filaments and molecular clouds, it would be more self-consistent to investigate how such asymmetric accretion flows from larger scales could affect disc formation (Kuffmeier, Haugbølle & Nordlund 2017; Kuznetsova, Hartmann & Heitsch 2020) under the regulation of non-ideal MHD effects.

5.4 Numerical limitations

Despite the dt floors we imposed for both AD and Hall effect, such floors are small enough and only trigger inside the disc or within the innermost <10 au (e.g. Fig. 6), where Ohmic dissipation already becomes very efficient so that the magnetic field strength saturates and the tendency of field bending by AD or Hall effect is suppressed (see detailed discussions in Paper I). As demonstrated in Zhao et al. (2018a), the process of disc formation is governed by the efficiency of magnetic diffusion and angular momentum transport outside (instead of inside) the disc, the dt floors used in the current study should not affect whether disc forms or not. Future zoom-in studies fully resolving the protoplanetary disc itself and magnetic diffusion therein are necessary to accurately follow the long-term disc evolution after the depletion of protostellar envelopes.

A missing aspect in this study is the self-consistent treatment of dust grains as separate fluids, which can result in important effects such as the spatial variation of dust-to-gas mass ratio due to aerodynamic drag (especially for grains of a few μm or larger; Hopkins & Lee 2016; Tricco, Price & Laibe 2017; Lebreuilly, Commerçon & Laibe 2020), and the spatial separation of different sized grains due to AD (Ciolek & Mouschovias 1996; Silsbee et al. 2020). We notice that Marchand et al. (2016) adopted a slightly higher dust-to-gas mass ratio of 0.0341 (reference model), hence we explore its effect on magnetic diffusivities in Fig. 17. For the given grain size range [0.0181, 0.9049] μm of Marchand et al. (2016), changing the dust-to-gas mass ratio from 0.0341 to 0.01 increases the diffusivities (both $\eta_{\rm AD}$ and $\eta_{\rm H}$) by a factor of a few at lower densities ($\lesssim$a few 10^9 cm^{-3}), while slightly reduces the diffusivities at higher densities (a few 10^9–10^{13} cm^{-3}). Basically, a larger dust-to-gas mass ratio yields higher abundance of small grains that dominates the fluid conductivity at low densities (Zhao et al. 2016; Dzyurkevich et al. 2017); it is only at high densities that efficient recombination due to the increased surface area starts to dominate. In comparison to our MRN case with grain size range [0.005, 0.25] μm and dust-to-gas mass ratio of 0.01, the reference model of Marchand et al. (2016) produces a somewhat lower $\eta_{\rm AD}$ at envelope densities (10^7–a few 10^{10} cm^{-3}), but a significantly larger (>1–2 orders of magnitude) $\eta_{\rm AD}$ close to the disc densities (a few 10^{10} cm^{-3}). Such a large $\eta_{\rm AD}$ (also for the Marchand 1 per cent case in Fig. 17) is likely the main reason for the 0.1 G plateau of magnetic field strength observed in Masson et al. (2016) and Hennebelle et al. (2016). Note that the

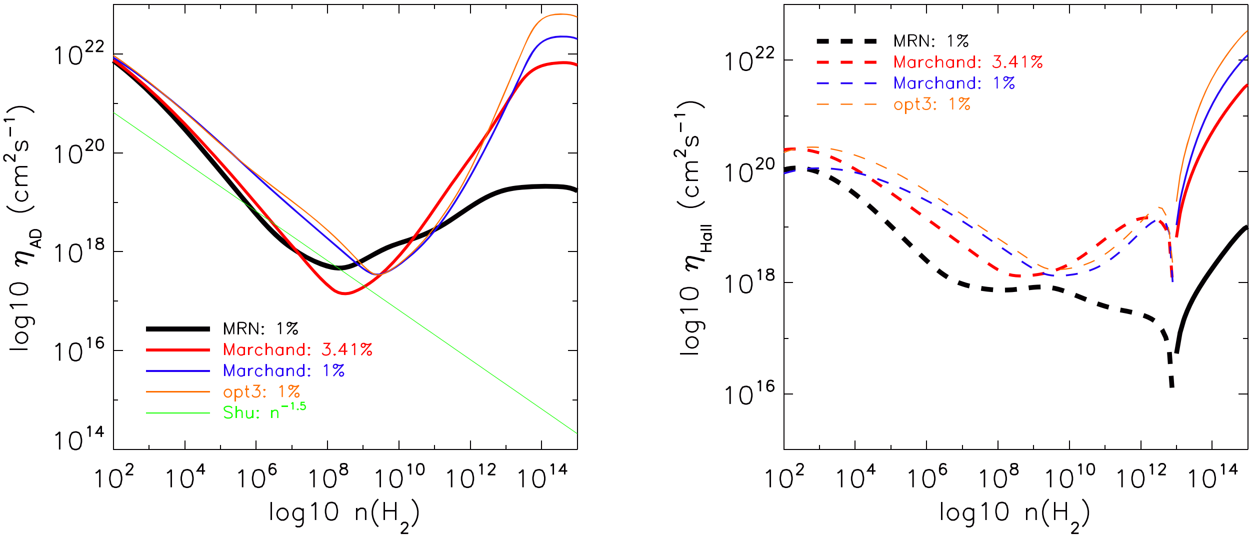

Figure 17. Effect of grain size distribution and dust-to-gas mass ratio on η_{AD} and η_{H}. In the reference model of Marchand et al. (2016), the grain size range is [0.0181, 0.9049] µm, and dust-to-gas mass ratio is 0.0341 (red curves). We also show a case using their size range but a standard dust-to-gas mass ratio 0.01 (blue curve). The MRN and opt3 cases adopted in this study with the size range [0.005, 0.25] µm are shown in black and orange curves. The fiducial level of η_{AD} of Shu (1991) is shown in green line. Note that a simple field strength–density relation is adopted with $|B| = 0.143 \left[\frac{\mathrm{n(H_2)}}{\mathrm{cm^{-3}}}\right]^{0.5}$ µG (Nakano, Nishi & Umebayashi 2002), along with our piecewise EOS (Section 3).

magnetic diffusivities of our opt3 case roughly match those of the ‘Marchand 1 per cent’ model in Fig. 17.

Finally, we have not considered radiative transfer in our non-ideal MHD models. As shown in recent studies (Tomida et al. 2013, 2015; Wurster & Bate 2019), the radiative transfer treatment is unlikely to determine whether or not discs can form, but will affect processes related to disc thermodynamics, such as disc stability and fragmentation, as well as centrifugal and spiral shocks. In fact, disc fragmentation in radiation hydrodynamic simulations appears to be resolution dependent (Forgan, Price & Bonnell 2017; Meyer et al. 2018), and thus quantitative convergence studies are still needed. Nevertheless, adopting a more realistic treatment of radiative transfer would better follow the compressional and shock heating near the disc edge (Sakai et al. 2014) and along spiral structures (Ilee et al. 2017) than using a simple barotropic EOS. Such sources of heating are critical for the disc chemical evolution, and could provide observational implications of the mass and temperature distributions in young discs (Zamponi et al., submitted).

6 SUMMARY

We have extended the study of Hall regulated disc formation in Paper I to a general case of disc formation enabled by non-ideal MHD effects. In particular, we have focused on the interplay between AD and Hall effect in the collapsing envelope, and the dependence on the magnetic field polarity and microphysics. We have found that, in spite of the non-trivial behaviours of the ambipolar and Hall drift, the combined effort of AD and Hall effect in the radial direction is to move the magnetic field radially outward relative to the infalling matter in the envelope, which greatly promotes the formation and survival of RSDs. Further conclusions are listed below.

1. We confirm the early result of Li et al. (2011) that disc formation is suppressed with the standard MRN size distribution ($a_{\min} = 0.005$ µm, $a_{\min} = 0.25$ µm), which results in a low Hall diffusivity within ≲100 au scale and a low ambipolar diffusivity at 10^2–10^3 au scale. Both the radial AD or the azimuthal Hall drift of magnetic fields are insufficient to enable disc formation.

2. Truncating the MRN size distribution at $a_{\min} \approx 0.03$ µm maximizes the Hall diffusivity in the inner envelope (≲100–200 au) and leads to a Hall-dominated collapse. RSDs of ∼20–30 au radii form regardless of the polarity of the magnetic field. However, the direction of disc rotation reverses as the magnetic field polarity flips: normally rotating for anti-aligned cases ($\boldsymbol{\Omega} \cdot \boldsymbol{B} < 0$) versus counterrotating for aligned cases ($\boldsymbol{\Omega} \cdot \boldsymbol{B} > 0$), with respect to the direction of initial core rotation.

3. For the Hall-dominated collapse, when $\boldsymbol{\Omega} \cdot \boldsymbol{B} > 0$, the radial components of both Hall and ambipolar drift are pointing towards $+r$, cooperatively diffusing the magnetic field radially outward. When $\boldsymbol{\Omega} \cdot \boldsymbol{B} < 0$, the radial Hall drift points towards $+r$ at 100 au scale but reverses to $-r$ at tens of au scale; however, the radial ambipolar drift along $+r$ always ensures the combined radial drift of the magnetic field relative to the bulk neutral matter is directed radially outward.

4. Further truncating the MRN size distribution at $a_{\min} \approx 0.1$ µm maximizes the ambipolar diffusivity throughout the collapsing envelope and leads to an AD-dominated collapse. Disc sizes and morphologies are largely unaffected by Hall effect in this case and hence independent of the magnetic field polarity. The radial drift of magnetic fields is primarily determined by AD, i.e. pointing radially outward; the azimuthal Hall drift is weakened due to the reduced radial pinching of poloidal magnetic fields by AD. Efficient AD of magnetic fields often results in self-gravitating discs that would become large spiral structures or multiple systems in a full 3D set-up.

5. Counterrotating envelope only develops in the Hall-dominated collapse, where Hall effect, by regulating the topology of the magnetic field, redistributes angular momentum among different parts of the envelope. Either a ‘butterfly-shaped’ thin shell is counterrotating (for $\boldsymbol{\Omega} \cdot \boldsymbol{B} < 0$), or the inner envelope enclosing the disc and outflow region is counterrotating (for $\boldsymbol{\Omega} \cdot \boldsymbol{B} > 0$). The aligned case also

shows a ‘butterfly-shaped’ thin shell with an excess of angular momentum.

6. With the help of Hall effect, the requirements on microphysics for disc formation are somewhat relaxed in comparison to studies focused only on AD. The lower limit of grain size $a_{\rm min}$ reduces from a few times 10 nm to just $\lesssim$10 nm; the upper limit of $\zeta_0^{\rm H_2}$ at the core scale increases from a few 10^{-17} to 2–3 $\times$ 10^{-16} $\rm s^{-1}$. Under such criteria, the majority of low-mass star-forming cores would allow RSDs to form. However, only compact discs of $\lesssim$10 au radius could form if the parent core has a relatively high CR ionization rate ($\zeta_0^{\rm H_2} \gtrsim 10^{-16}$ $\rm s^{-1}$).

7. The polarity of the magnetic field can also affect the disc to stellar mass ratio and hence the disc stability in the Hall-dominated collapse; the aligned case tends to grow a large stellar mass during its initial disc suppression phase.

8. In the aligned case, outflow cavity is generally wider and outflow speed is a few times faster than in the anti-aligned case, due to the strengthening of B_ϕ by the azimuthal Hall drift. The Hall-dominated collapse ($a_{\rm min} \approx 0.03$ μm) also launches stronger outflows than the AD-dominated collapse ($a_{\rm min} \approx 0.1$ μm), as poloidal magnetic fields are weaker and less pinched when AD is strong.

9. Hall effect is only efficient in spinning up/down the gas rotation in relatively strongly magnetized cores. For $\lambda \gtrsim 10$, the azimuthal Hall drift is negligible even when adopting $a_{\rm min} \approx 0.03$ μm.

10. In general, if ambipolar and Hall drift are cooperative in a given direction (r- or ϕ- direction), they are counteractive in the orthogonal direction (ϕ- or r- direction). Such a principle can be applied to either a collapsing envelope or a rotating disc, with magnetic field lines being preferentially pinched radially by collapse in the former while bended azimuthally by rotation in the latter. The combined effect of AD and Hall effect is to drift the magnetic field against the primary direction of field bending.

11. The sign of $\boldsymbol{\Omega} \cdot \boldsymbol{B}$ of protoplanetary discs are closely related to the microphysics in the protostellar envelope; only the anti-aligned configuration is possible for discs formed from a Hall-dominated collapse, whereas both aligned and anti-aligned configurations are allowed for discs formed from an AD-dominated collapse.

We conclude that the strong dependence of non-ideal MHD effects on microphysics places microphysics in a pivotal role in protostellar collapse and disc formation. The depletion of VSGs below $\lesssim$10 nm in prestellar cores remains critical for promoting disc formation. Slight changes in microphysics can leave profound imprints on observables, including rotation direction of envelopes and discs, size, and morphology of discs, velocity, and open-angle of outflows, and possibly disc to stellar mass ratio. Although most of these detailed features are related to Hall effect and the magnetic field polarity, AD remains as the cornerstone for disc formation and survival by ensuring a radially outward diffusion of the magnetic field in the collapsing envelope.

ACKNOWLEDGEMENTS

BZ and PC acknowledge support from the European Research Council (ERC; project PALs 320620) and the Max-Planck Society. Z-YL and K-HL are supported in part by NASA (80NSSC18K1095, 80NSSC20K0533) and NSF (1716259). HS and RK acknowledge grant support from the ASIAA and the Ministry of Science and Technology in Taiwan through MOST 105-2119-M-001-037- and 105-2119-M-001-044-MY3. ZEUSTW is developed and maintained by the CHARMS group in ASIAA. Numerical simulations are carried out on the CAS group cluster at MPE.

DATA AVAILABILITY

The simulation data underlying this article are available on request from the corresponding author, Bo Zhao.

REFERENCES

Allen A., Li Z.-Y., Shu F. H., 2003, ApJ, 599, 363
Bai X.-N., Stone J., 2017, ApJ, 836, 46
Ballering N. P., Eisner J. A., 2019, AJ, 157, 144
Bergin E. A., Tafalla M., 2007, ARA&A, 45, 339
Béthune W., Lesur G., Ferreira J., 2017, A&A, 600, 75
Blandford R. D., Payne D. G., 1982, MNRAS, 199, 883
Braiding C. R., Wardle M., 2012, MNRAS, 422, 261
Braiding C. R., Wardle M., 2012, MNRAS, 427, 3188
Caselli P., Walmsley C. M., Terzieva R., Herbst E., 1998, ApJ, 499, 234
Caselli P., Walmsley C. M., Zucconi A., Tafalla M., Dore L., Myers P. C., 2002, ApJ, 565, 344
Caselli P., Benson P. J., Myers P. C., Tafalla M., 2002, ApJ, 572, 238
Ciolek G. E., Mouschovias T. Ch., 1996, ApJ, 468, 749
Dapp W. B., Basu S., Kunz M. W., 2012, A&A, 541, 35
Dzyurkevich N., Commerçon B., Lesaffre P., Semenov D., 2017, A&A, 603, 105
Forgan D., Price D. J., Bonnell I., 2017, MNRAS, 466, 3406
Fuller G. A., Myers P. C., 1992, ApJ, 384, 523
Goodman A. A., Benson P. J., Fuller G. A., Myers P. C., 1993, ApJ, 406, 528
Gressel O., Turner N. J., Nelson R. P., McNally C. P., 2015, ApJ, 801, 84
Guillet V., Hennebelle P., Pineau des Forêts G., Marcowith A., Commerçon B., Marchand P., 2020, A&A, 643, 17
Hennebelle P., Fromang S., 2008, A&A, 477, 9
Hennebelle P., Commerçon B., Chabrier G., Marchand P., 2016, ApJ, 830, 8
Hennebelle P., Commerçon B., Lee Y.-N., Charnoz S., 2020, A&A, 635, 67
Hirashita H., 2012, MNRAS, 422, 1263
Hopkins P. F., Lee H., 2016, MNRAS, 456, 4174
Ilee J. D. et al., 2017, MNRAS, 472, 189
Joos M., Hennebelle P., Ciardi A., 2012, A&A, 543, 128
Keto E., Caselli P., 2008, ApJ, 683, 238
Koga S., Tsukamoto Y., Okuzumi S., Machida M. N., 2019, MNRAS, 484, 2119
Köhler M., Stepnik B., Jones A. P., Guillet V., Abergel A., Ristorcelli I., Bernard J.-P., 2012, A&A, 548, 61
Krasnopolsky R., Königl A., 2002, ApJ, 580, 987
Krasnopolsky R., Li Z.-Y., Shang H., 2010, ApJ, 716, 1541
Krasnopolsky R., Li Z.-Y., Shang H., 2011, ApJ, 733, 54
Krasnopolsky R., Li Z.-Y., Shang H., Zhao B., 2012, ApJ, 757, 77
Kuffmeier M., Haugbølle T., Nordlund Å., 2017, ApJ, 846, 7
Kuffmeier M., Zhao B., Caselli P., 2020, A&A, 639, 86
Kunz M. W., 2008, MNRAS, 385, 1494
Kuznetsova A., Hartmann L., Heitsch F., 2020, ApJ, 893, 73
Lam K.-H., Li Z.-Y., Chen C.-Y., Tomida K., Zhao B., 2019, MNRAS, 489, 5326
Larson R. B., 1969, MNRAS, 145, 271
Lebreuilly U., Commerçon B., Laibe G., 2020, A&A, 641, A112
Lesur G., 2020, preprint (arXiv:2007.15967)
Li Z.-Y., McKee C. F., 1996, ApJ, 464, 373
Li Z.-Y., Krasnopolsky R., Shang H., 2011, ApJ, 738, 180
Li Z.-Y., Krasnopolsky R., Shang H., 2013, ApJ, 774, 82
Li Z.-Y., Krasnopolsky R., Shang H., Zhao B., 2014, ApJ, 793, 130
Machida M. N., Basu S., 2020, MNRAS, 494, 827
Machida M. N., Inutsuka S.-I., Matsumoto T., 2007, ApJ, 670, 1198
Machida M. N., Inutsuka S., Matsumoto T., 2014, MNRAS, 438, 2278
Manara C. F., Morbidelli A., Guillot T., 2018, A&A, 618, 3

Marchand P., Masson J., Chabrier G., Hennebelle P., Commerçon B., Vaytet N., 2016, A&A, 592, 18
Marchand P., Commerçon B., Chabrier G., 2018, A&A, 619, A37
Marchand P., Tomida K. Tanaka K. E. I., Commerçon B., Chabrier G., 2020, ApJ, 900, 180
Masson J., Chabrier G., Hennebelle P., Vaytet N., Commerçon B., 2016, A&A, 587, 32
Mathis J. S., Rumpl W., Nordsieck K. H., 1977, ApJ, 217, 425
Mellon R. R., Li Z.-Y., 2008, ApJ, 681, 1356
Mellon R. R., Li Z.-Y., 2009, ApJ, 698, 922
Meyer D. M.-A., Kuiper R., Kley W., Johnston K. G., Vorobyov E., 2018, MNRAS, 473, 3615
Nakano T., Nishi R., Umebayashi T., 2002, ApJ, 573, 199
Ossenkopf V., 1993, A&A, 280, 617
Padovani M., Galli D., Glassgold A. E., 2009, A&A, 501, 619
Padovani M., Galli D., Hennebelle. P., Commerçon B., Joos M., 2014, A&A, 571, 33
Padovani M., Ivlev A. V., Galli D., Caselli P., 2018, A&A, 614, 111
Pelletier G., Pudritz R. E., 1992, ApJ, 394, 117
Pineda J. E. et al., 2020, Nat. Astron., 4, 1158
Sakai N. et al., 2014, Nature, 507, 78
Santos-Lima R., de Gouveia Dal Pino E. M., Lazarian A., 2012, ApJ, 747, 21
Segura-Cox D. M. et al., 2018, ApJ, 866, 161
Seifried D., Pudritz R. E., Banerjee R., Duffin D., Klessen R. S., 2012, MNRAS, 422, 347
Seifried D., Banerjee R., Pudritz R. E., Klessen R. S., 2013, MNRAS, 432, 3320
Shu F. H., 1991, Physics of Astrophysics, Vol. II: Gas Dynamics. University Science Books, New York
Shu F. H., Galli D., Lizano S., Cai M., 2006, ApJ, 647, 382
Silsbee K., Ivlev A., Caselli P., Sipila O., Zhao B., 2020, A&A, 641, A39
Suriano S. S., Li Z.-Y., Krasnopolsky R., Shang H., 2018, MNRAS, 477, 1239
Takakuwa S., Tsukamoto Y., Saigo K., Saito M., 2018, ApJ, 865, 51
Takasao S., Tomida K., Iwasaki K., Suzuki T. K., 2018, ApJ, 857, 4
Tibbs C. T. et al., 2015, MNRAS, 456, 2290
Tobin J. J. et al., 2016, ApJ, 818, 73
Tomida K., Tomisaka K., Matsumoto T., Hori Y., Okuzumi S., Machida M. N., Saigo K., 2013, ApJ, 763, 6
Tomida K., Okuzumi S., Machida M. N., 2015, ApJ, 801, 117
Tomisaka K., 2002, ApJ, 575, 306
Tricco T. S., Price D. J., Laibe G., 2017, MNRAS, 471, 52
Troland T. H., Crutcher R. M., 2008, ApJ, 680, 457
Tsukamoto Y., Iwasaki K., Okuzumi S., Machida M. N., Inutsuka S., 2015, MNRAS, 452, 278
Tsukamoto Y., Iwasaki K., Okuzumi S., Machida M. N., Inutsuka S., 2015, ApJ, 810, 26
Tsukamoto Y., Okuzumi S., Iwasaki K., Machida M. N., Inutsuka S., 2017, PASJ, 69, 95
Tsukamoto Y., Machida M. N., Susa H., Nomura H., Inutsuka S., 2020, ApJ, 896, 158
Umebayashi T., Nakano T., 1990, MNRAS, 243, 103
Wardle M., Ng C., 1999, MNRAS, 303, 239
Wurster J., Bate M. R., 2019, MNRAS, 486, 2587
Wurster J., Li Z.-Y., 2018, Front. Astron. Space Sci. , 5, 39
Wurster J., Price D. J., Bate M. R., 2016, MNRAS, 457, 1037
Wurster J., Price D. J., Bate M. R., 2017, MNRAS, 466, 1788
Xu R., Bai X.-N., 2016, ApJ, 819, 68
Yen H.-W. et al., 2019, ApJ, 871, 243
Yen H.-W. et al., 2020, ApJ, 893, 54
Zhao B., Li Z.-Y., Nakamura F., Krasnopolsky R., Shang H., 2011, ApJ, 742, 10
Zhao B., Caselli P., Li Z.-Y., Krasnopolksy R., Shang H., Nakamura F., 2016, MNRAS, 111, 22
Zhao B., Caselli P., Li Z.-Y., Krasnopolksy R., 2018, MNRAS, 473, 4868
Zhao B., Caselli P., Li Z.-Y., 2018, MNRAS, 478, 2723
Zhao B., Caselli P., Li Z.-Y., Krasnopolksy R., Shang H., Lam K.-H., 2020, MNRAS, 492, 3375 (Paper I)

APPENDIX: CHEMISTRY NETWORK

As the microphysics plays a crucial role in the non-ideal MHD processes in protostellar collapse and disc formation, we briefly describe the chemical network used for obtaining the magnetic diffusivities in the study. Such information would facilitate cross-comparisons with other non-ideal MHD studies of protostellar collapse.

As described in Zhao et al. (2018b), the reduced chemical network includes 21 neutral species, 31 ion species, and neutral and singly charged grain species, as well as electrons. We consider mainly gas-phase reactions; dust grains participate in the ion and electron recombination, charge transfer, and molecular freeze-out and desorption reactions. Due to the efficient freeze-out of CO molecules in the protostellar envelope, H_3^+ becomes the dominant ion species, instead of HCO^+. The freeze-out effect also slightly suppresses the corresponding ion species in the gas phase and thus slightly increases the magnetic diffusivities in the inner envelope (Zhao et al. 2018b; Paper I). Similar to our previous work, we choose a low metal abundances (Fe and Mg) $\lesssim 10^{-8}$, consistent with the level of metal depletion estimated in dense core environments (Caselli et al. 2002a). Finally, the dust-to-gas mass ratio is fixed at 0.01 in the chemical network; as a result, varying the grain size distribution will change the average abundance and total surface area of grains.

This paper has been typeset from a TEX/LATEX file prepared by the author.